

Contents lists available at [ScienceDirect](https://www.sciencedirect.com)

Mechanical Systems and Signal Processing

journal homepage: www.elsevier.com/locate/ymssp

The surrogate system hypothesis for joint mechanics

Nidish Narayanaa Balaji, Matthew R.W. Brake*

Department of Mechanical Engineering, Rice University, Houston, TX 77005, United States

ARTICLE INFO

Article history:

Received 11 September 2018

Received in revised form 17 December 2018

Accepted 8 February 2019

Available online 16 February 2019

Keywords:

Joint mechanics

Friction modeling

Multi-Objective Optimization

ABSTRACT

The main challenges in the design and analysis of jointed structures deal with the prediction of dissipation across bolted interfaces. Since friction is thought to be one of the main mechanisms for this, the current study investigates the utility of frictional parameter identification applied across different structures. Based on recent discoveries, a Surrogate System Hypothesis has been formulated to systematize this: the hypothesis states in brief, that the physical properties of a joint are independent of its structural context. The current work seeks to obtain a better understanding of the underlying systems by evaluating a confidence metric for the hypothesis for a relatively simple set of systems—physically perturbed configurations of the Brake-Reuß Beam. Interfacial friction is modeled using whole jointed patches with distributed hysteretic (Iwan) elements and simulations are conducted using the Quasi-Static Modal Analysis (QSMA) approach to estimate the modal characteristics of the system response (amplitude dependence of natural frequency and dissipation). Posing the estimation as a Multi-Objective Optimization Problem (MOOP) is shown to reveal important features of both the employed constitutive model as well as the structure that is modeled. Consequently, the approach is used to evaluate the epistemic uncertainty inherent in three different friction models. The studies reveal that a confidence metric for the hypothesis can be formulated in such a way that it is nearly independent of the friction constitutive model that is employed.

© 2019 Published by Elsevier Ltd.

1. Introduction

Despite the pervasiveness of mechanical joints in assembled structures, the lack of accurate predictive models for such systems has remained a persistent issue for the community. This is primarily due to the lack of knowledge of the physics governing interfacial interactions, resulting in predictions of energy transmission/dissipation through interfaces being often in error by several orders of magnitude [50,8]. The major difficulty in developing accurate computational models lies in the multi-scale nature of interfacial interactions. Friction, for instance, whose effects are perceivable in the macro-scale, is thought to be a phenomenon that is fundamentally established by the micro-scale properties of the interfaces. Refining the model to include micro-scale irregularities has two major challenges: (1) uncertainty in the characterization of the interface, and (2) computational cost. Efforts are being made to improve on both aspects in order to make joint modeling feasible. Regarding the first challenge, there are multiple studies addressing issues in rough contact [26,20,19], validating hysteresis measurement techniques [21], and developing methods of relating them to surface roughness, leading eventually to more detailed constitutive models for friction [6]. Experimental characterization is often used to develop fully- or semi-empirical models by using experimental measurements for parameter estimation [46,45].

* Corresponding author.

E-mail addresses: nb25@rice.edu (N.N. Balaji), brake@rice.edu (M.R.W. Brake).

Nomenclature

C	linear viscous damping matrix
K	linear stiffness matrix
M	linear inertia matrix
\dot{q}	time derivative of quantity q
ϵ	design success tolerance
η_0^k	k th low amplitude mode weight (modal coordinate)
ω_0^k	k th low amplitude mode frequency
ω_n	natural frequency
ϕ_0^k	k th low amplitude mode shape
$\psi(t)$	phase at time t
θ	stiction ratio
ζ_n	linear damping factor
$A(t)$	displacement amplitude at time t (“low-pass”)
D	dissipation across frictional element
$f(t)$	linear non-homogeneous forcing
F_k^l	contribution of l th low amplitude modal forcing to k th low amplitude modal forcing
F_S	slipping force
F_{NL}	nonlinear forcing
j	complex quantity $\sqrt{-1}$
K_0	stress-stiffness matrix
K_A	stress-augmented stiffness matrix
K_b	bolt stiffness of bolted structure
K_m	member stiffness of bolted structure
K_T	low amplitude sticking stiffness
K_Z	Z-(normal) directional stiffness
$L_\infty(q)$	L_∞ deviation between predicted and experimented values of q
R, S, ϕ_{max}, χ	parameters of the four-parameter Iwan Model
$u(t)$	displacement at time t (“high-pass”)
u_k^l	contribution of l th low amplitude modal displacement to k th low amplitude modal forcing response
ANOVA	ANalysis Of VAriance
BRB	nominal Brake-Reuß beam
DOF	degree-of freedom
LBRB	length-modified Brake-Reuß beam
MOOP	multi-objective optimization problem
MPC	multi-point constraint
QSMA	Quasi-Static Modal Analysis
SBRB	stiffness-modified Brake-Reuß beam

The second challenge presents an imminent problem from a system-level perspective since it is not computationally feasible to develop models of large systems refined to very small length-scales. Efforts have been focused both on multi-scale modeling [3,40] as well as the application of interface reduction techniques [34,43,24] & nonlinear reduced order modeling [28]. Common solution techniques applied to the analysis of structures include the time integration technique and the harmonic balance method. Time integration tends to be inefficient for large built-up structures [25], since jointed structures, being lightly damped, will have to be integrated for a long time to sufficiently remove the effect of transients. On the other hand, the harmonic balance method, based on a truncated asymptotic series expansion in the frequency domain, offers a faster way to calculate steady state responses [11,41,44]. However, both of these techniques prove to be computationally expensive for even small assemblies such that they present a significant limitation in the application of system identification techniques, which are primarily developed for simpler geometries [1] (see [32,33,39,25] for a review of the state-of-the-art in such methods). Even if the methods are adapted for real-world structures, adapting the methods will require in situ joint characterization. Since this involves the fabrication of the complete system, it renders any design optimization prohibitively expensive. In part, this is due to a lack of understanding of the interaction between the joint and its structural context. Although there has been at least one experimental study [13] in this direction, it is still not entirely clear how nominally identical joints can be expected to behave in dissimilar structures. It is presupposed that the far-field structure will influence the loading of the joint leading to different response characteristics [5]. The current work attempts to assess the possibility of using a joint parameter set estimated from one structure to model a nominally identical joint in another. This is intended to potentially enable engineers to develop models based on lab-scale experimental structures to be applied for the design of real world structures.

The amplitude dependence of modal parameters (frequency and dissipation) are used as the primary metric for the characterization of nonlinearities in the current work. [23] developed a technique to study the behavior of perturbed linear modes of a system in the presence of interfacial nonlinearity using quasi-static simulations alone. The low amplitude linear mode shapes are incrementally updated in order to obtain modal behavior at higher amplitudes, leading to efficient calculation of nonlinear amplitude dependence of modal parameters. [2] suggested a further reduction, based on the assumption that the changes in the mode shapes are negligible in the operating ranges of interest for bolted joints. Complementing this, a theorem due to [51] may be used to prove that perturbations in viscous damping only leads to second order changes in the mode shapes of mechanical systems. This was further extended in [42] to study the effects of non-viscous damping terms in the system.

As in [37], this method is formally presented as Quasi-Static Modal Analysis (QSMA). Due to its computational efficiency, it is possible to conduct more *diverse* searches in the parameter-space for empirical model parameter estimation. A persisting challenge, however, is the determination of model parameters for a selected constitutive model. Even for simple models, such as Coulomb friction or an elastic dry-friction (or *Jenkins*) element, measurements indicate a wide range of potentially correct model parameters [27]. Recently, this has been treated as an optimization problem in a model updating context [36]. In Kuether and Najera[35], the authors have attempted this challenge by using a genetic algorithm implementation to estimate the parameters for Segalman's four-parameter Iwan model [49] applied to a prestressed interface undergoing tangential excitation. A limitation of this study is that the estimation problem was reduced into a single objective optimization framework by weighting the errors in the frequency and the dissipation (damping factor) to obtain a single optimization metric. Although mathematically valid, this approach misses out on various features of the underlying multi-objective problem (MOOP) [15]. The current work uses a more direct error metric in each modal parameter and attempts to look at the estimation as a bi-objective optimization problem. It is shown that this standpoint enables one to extract relative features between pairs of systems in ways that are thought to be relatively independent of the model. Starting with the premise that when the model has associated epistemic uncertainties, families of optimal models are sought and studied in the parameter-space instead of seeking a unique optimal model to fit the experimental observations. Intersections of such families in the parameter-space identified from different systems is hypothesized to be influenced more by the nature of the systems themselves than the fitting model. The current paper presents numerical explorations of this idea, bringing out results for the different Brake-Reuß Beam configurations considered in [13] and outlining possible shortcomings.

The remainder of the paper is organized as follows: Section 2 introduces the statement of the surrogate system hypothesis, Section 3 gives a brief overview of the different beam configurations for the current study, Section 4 provides the theoretical background for the computational aspects, Section 5 provides the numerical results for the systems under consideration and Sections 6,2,3,4,5,6,7 outline the major takeaways as well as shortcomings of the current approach and how they relate to the surrogate system hypothesis. Lastly, Section A presents the engineering drawings of the different systems under investigation.

2. The surrogate system hypothesis

The surrogate system hypothesis states that *the physical properties of a joint are independent of its structural context*. As a corollary to this, the hypothesis implies that a joint characterized in one assembly can be directly used to predict the response of a different system with the same joint. It must be noted that this may be treated as fairly trivial for linear components. For example, a linear spring is modeled as adding the same stiffness to the system irrespective of its disposition in a dynamical system. However, the historical perspective on frictional components is that the system and the joint response are fully convoluted. There have even been a few experimental studies discouraging a fully disconnected view (see, for example [5]). This presents a conceptual difficulty in interpreting experimental data in the context of the performance of a real structure. More than proving the hypothesis, evaluating a confidence in its validity can be a means of providing a better understanding of the underlying system.

For the purposes of the current investigation, a *real system* is defined as any structure of interest with one or more jointed interfaces, and a *surrogate system* is defined as a structure with a single jointed interface identical to one of the joints in the real system. For instance, N different surrogate structures may be defined for a real system with N characteristically different joints. The surrogate structures are carefully constructed laboratory models with just a single source of non-linearity: it's focal joint. As a starting point, all of the real structures considered here consist of just a single joint.

3. Systems of investigation

Fig. 1 presents schematic diagrams of three configurations of the Brake-Reuß Beams (BRBs) considered in [13] (see Section A for engineering drawings). The nominal beam (BRB) consists of a pair of stepped beams bolted together through a three-bolt lap joint. The other two configurations are physically perturbed designs of the BRB—the stiffness-modified beam (SBRB), with far-field spring-like structures, and the length-modified beam (LBRB), with longer beams on either side. It must be noted that the joint interfaces are geometrically congruent in all three structures, without any scaling applied. Further, identical bolt torques (excluding experimental uncertainty) as well as assembly procedures are followed during the assembly of all the structures.

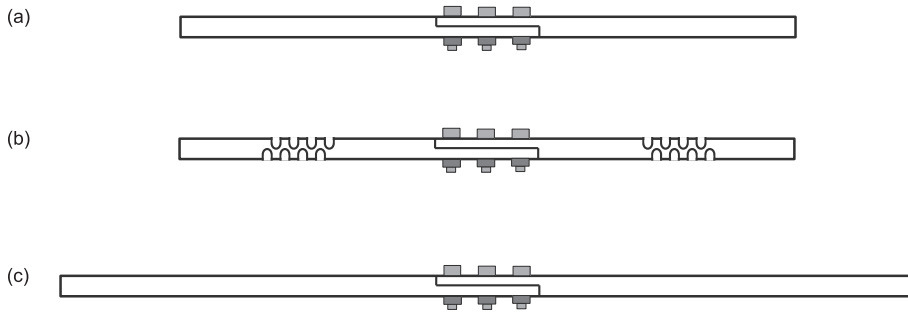


Fig. 1. Three different configurations of the Brake-Reuß Beam: (a) Nominal (BRB), (b) Spring-modified (SBRB), and (c) Length-modified (LBRB) [13].

3.1. Experimental characterization

The beams are suspended using bungee wires, in order to best realize fully free boundary conditions. With ten accelerometers positioned along the beam, low impact hammer tests are used to extract the low amplitude mode-shapes experimentally (see [13] for results of this). A schematic of the experimental setup used for the BRB is depicted in Fig. 2. Following this, accelerometer data from higher amplitude hammer tests (ring down acceleration data) are transformed, using the experimental mode shapes, to modal amplitudes. Then, a Hilbert transform method, based on the “FreeVib” procedure outlined in [22], is used to obtain instantaneous modal amplitude, frequency and damping ratio estimates. Using the Hilbert transform, any ring-down signal may be decomposed into an envelope and a phase (both real-valued functions of time) as

$$\begin{aligned}
 u(t) &= A(t)\cos(\psi(t)) \\
 &= \text{Re}\{A(t)e^{j\psi(t)}\}.
 \end{aligned}
 \tag{1}$$

A quasi-linear approximation is realized by setting the displacement variation (the “high-pass”, or high-frequency response component) to be governed by a linear second order dynamical equation retaining the dependence of the coefficients only on the response amplitudes (the “low-pass”, or low-frequency response component). Mathematically, the governing equation is given as

$$\ddot{u} + 2\zeta_n(A)\omega_n(A)\dot{u} + \omega_n(A)^2 u = 0,
 \tag{2}$$

where $\omega_n(A)$ and $\zeta_n(A)$ represent the natural frequency and damping factor as functions of the response envelope amplitude A . From linear theory for under-damped systems, the general solution of this may be expressed by

$$u(t) = u_0 e^{-\zeta_n \omega_n t} e^{-j(\omega_n \sqrt{1-\zeta_n^2} t + \phi)},
 \tag{3}$$

with u_0 and ϕ determining the initial conditions. Using the Hilbert transform functions $A(t)$ and $\psi(t)$ in conjunction with the quasi-linear solution, it is possible to obtain the modal properties as follows:

$$\begin{aligned}
 \omega_n(t) &= \sqrt{\left(\frac{d\psi(t)}{dt}\right)^2 + \left(\frac{d}{dt} \log A(t)\right)^2} \approx \frac{d\psi(t)}{dt} \\
 \zeta_n(t) &= -\frac{1}{\omega_n} \frac{d \log A(t)}{dt}
 \end{aligned}
 \tag{4}$$

Table 1 summarizes the natural frequency and linear damping ratio at the low amplitude levels for the first bending mode in the structure. It can be observed that different low amplitude damping factors are measured for each beam.

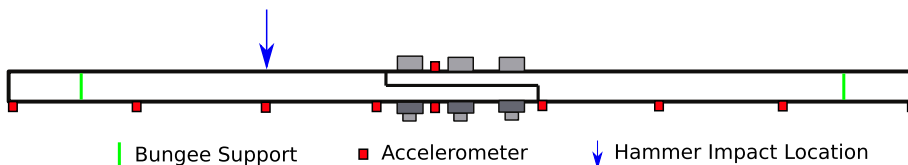


Fig. 2. Experimental Setup (BRB): Red squares represent locations of accelerometers; Green lines represent the locations of suspension (using bungee cords), and the blue arrow indicates the point of hammer input [13]. (For interpretation of the references to colour in this figure legend, the reader is referred to the web version of this article.)

Table 1
Mean low amplitude modal parameters for the first out-of-plane bending mode of the different beam configurations.

Beam	Frequency (Hz)	Damping factor ($\times 10^{-6}$)
BRB	169.48	1665.9340
LBRB	80.82	924.3096
SBRB	91.96	946.0959

Fig. 3 shows the results of the experimental studies indicating the deviations of the natural frequencies and damping factors from their low-amplitude values (given in Table 1) as functions of their modal displacement amplitudes. The data are averaged from Hilbert transform fits on transient ring-down responses of seven independent hammer tests (without disassembly).

The decreasing trends in the natural frequencies and the increasing trends in the damping factors are typical of a jointed system [54]: the system is “fully stuck” at low amplitudes, with maximal stiffness across the interface, and “partially slipped” at higher amplitudes, with reduced interfacial stiffness. Looking at the frequency deviations, it can be seen that the behaviors of the BRB and the LBRB almost line up against each other while the deviations for the SBRB are much lesser. The maximal deviations in the natural frequencies of the models due to nonlinearity are approximately 2%. The damping factor deviations show more perceivable nonlinear effects in the large increase with the modal amplitude. The deviations in the SBRB are much lesser in comparison with the other two beams but none of the curves seem to fall on top of each other. The main inference from these curves is that among the three structures, the SBRB is the one that is *most linear*. There is some similarity between the BRB and the LBRB but no conclusive statement may be made of this since the interface loading conditions are fundamentally different.

4. Modeling approach

4.1. Structural modeling

The structural modeling uses the finite element mesh¹ (a view of the mesh at the interface is depicted in Fig. 4b) that was presented in [36]. Following the generation of the finite element mesh, a prestress analysis is conducted to capture the residual stresses in the structure due to bolting it together. The augmented stiffness matrices (augmented in terms of including the prestress effects) are then exported for the nonlinear analysis.

For modeling the bolted lap joint, Lacayo et al. [36] considered different interface representations. Owing to its computational advantages, the “whole-joint” approach [7] is used in the current study. As depicted in Fig. 4a, the interface is divided into five patches (note that the grids here denote just the physical partitions in the model and not the underlying mesh. See Fig. 4b for the interfacial mesh.). The displacements and rotations of each of these patches is coupled to a virtual node with six degrees-of-freedom (DOFs). A set of multi-point constraints (MPCs) are formulated to set each DOF of the virtual node to the average of the nodes in its corresponding patch. This procedure is not the same as rigidly tying all the nodes of the patch together, as normal compliance is introduced via linear springs in the z-direction.

In order to model the interfacial nonlinearities, pairs of virtual nodes from corresponding patches are connected using normal and tangential constitutive models. By contrast, node-to-node contact is much more expensive as every node on the interface is associated with a corresponding node on the opposite face using a frictional constitutive model. The node to node approach, although being more accurate, is prohibitively expensive in terms of computational requirements for conducting analyses in the current spirit. [24] considers the impacts of some design decisions that may be useful to strike a common ground between the two approaches.

Finite element models of the three beams are developed in ABAQUS with appropriate virtual nodes introduced for interface reduction. Since these are bolted connections and all of the experimental data presented in Section 3 were from assemblies with bolts torqued to approximately 20 N m, the equivalent bolt prestress force (calculated to 11,580 N for steel bolt-washer-nuts, see [10]) is applied to the model. The material properties for all the components are modeled as linear isotropic materials, with a Young’s modulus of 190 GPa, and a Poisson’s ratio of 0.29.

As stated above, static prestress analysis is first conducted on the full structure with a frictionless “hard” (no-penetration) contact in order to obtain the interfacial normal pressure distribution. The solution in this step is used to construct a stress stiffness matrix, which is augmented to the original stiffness matrix to represent the dynamical system about the prestressed state (see [12] for examples). The incremental normal contact displacements about this state is modeled as being stiffened by a linear spring. This is justified by the fact that the magnitudes of excitation are expected to produce negligible changes in the interfacial normal pressures. Thus each patch will have an unknown normal stiffness parameter in addition to the frictional parameters that will have to be estimated through the design exploration. The current model does not capture the

¹ Details of the convergence study for this converged mesh are omitted here, and the interested reader is referred to [36] and its references.

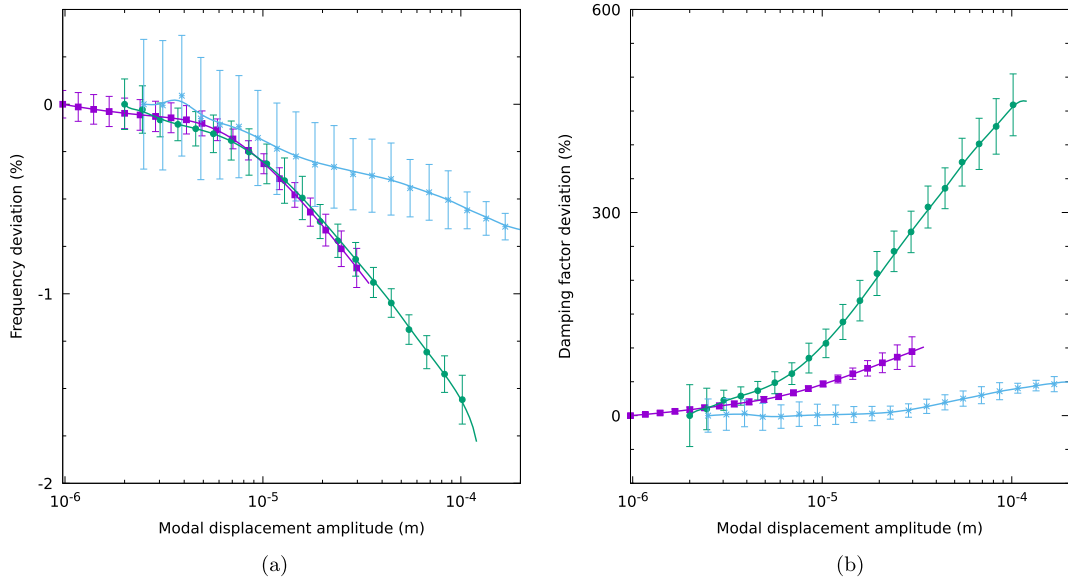


Fig. 3. Experimental (a) frequency and (b) damping factor deviations from low-amplitude values, shown for the BRB (—■—), LBRB (—●—), and the SBRB (—*—).

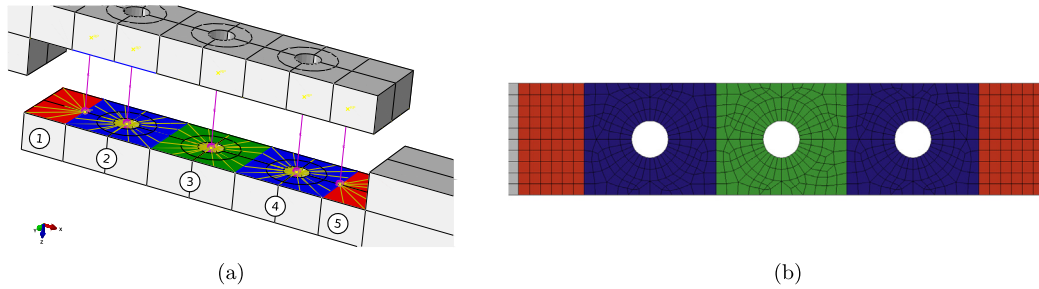


Fig. 4. (a) The five-patch whole-joint interface with correspondingly labeled regions, and (b) a view of the finite element mesh at the interface. By symmetry, regions 1 and 5 are taken to have identical properties, as well as regions 2 and 4.

kinematics of interfacial separation. For a more accurate study, better-suited normal contact formulations (like [38], for example), must be adopted. But this will come at the cost of additional computational burden for the investigation. Following this, a Hurty/Craig-Bampton fixed-interface component mode dynamic substructuring [29,14] is conducted, retaining all of the degrees of freedom of the interface nodes (6 DOFs × 10 virtual nodes: 60 boundary DOFs) and 26 fixed interface component modes to give a reduced system that is capable of capturing up to the first four bending modes of the beams accurately.

4.2. Quasi-Static Modal Analysis

QSMA [37] is a simplification of the quasi-static analysis method expounded in [23]. The basic ideas of the procedure is outlined here to bring out the essential principles of the approach.

The approach assumes a dynamic system of the form

$$\mathbf{M}\ddot{\mathbf{u}} + \mathbf{C}\dot{\mathbf{u}} + \mathbf{K}\mathbf{u} + F_{NL}(\mathbf{u}, \dot{\mathbf{u}}, \dots) = \mathbf{f}(t), \tag{5}$$

with matrices \mathbf{M} , \mathbf{C} , and \mathbf{K} denoting the inertial, viscous damping and linear stiffness matrices respectively; \mathbf{u} denoting the vector of degrees of freedom, and $F_{NL}(\mathbf{u}, \dot{\mathbf{u}}, \dots)$ and $\mathbf{f}(t)$ denoting the nonlinear state-dependent forcing and the non-autonomous excitation terms respectively. Note that no time dependence is considered in F_{NL} since all of the friction models considered in the current work are fully autonomous in their formulation.

The nonlinear forcing terms from the interfacial friction are such that the forces are zeros when the displacements are zero, i.e., $F_{NL} \rightarrow 0$ in the limit of $u_i \rightarrow 0$. For hysteretic models, this represents the backbone curve (see Section 4.3). Some

of these models contribute a finite stiffness for small displacement amplitudes, represented by \mathbf{K}_0 . Thus, the low amplitude form of eq. (5) is

$$\mathbf{M}\ddot{\mathbf{u}} + \mathbf{C}\dot{\mathbf{u}} + \overbrace{[\mathbf{K} + \mathbf{K}_0]}^{K_A} \mathbf{u} = f(t), \quad (6)$$

which has the augmented low amplitude stiffness matrix K_A . Being a fully linear system, the homogeneous part ($f(t) = 0$) may be decomposed into its oscillatory modes ω_0^k and corresponding mode shapes ϕ_0^k , with k denoting modal index. For sufficiently underdamped systems the mode shapes may be approximated to a second order accuracy as exponentially decaying undamped mode shapes [51]. The undamped mode shapes consist of all of the DOFs oscillating in phase with one another, i.e., the mode shape may be expressed as real vectors in a discretized model. Using modal summation to represent the solution as a linear combination of the mode shapes we have,

$$\mathbf{u}_L(t) = \sum_{k=0}^N \eta_0^k \phi_0^k e^{j\omega_0^k t}. \quad (7)$$

Here, j denotes the complex quantity $\sqrt{-1}$, and η_0^k represents the contribution of a particular mode to the solution. Being a self-adjoint system, the non-degenerate mode shapes are orthonormalized with respect to the inner product,

$$\langle \phi_0^l, \phi_0^k \rangle = \phi_0^{lT} \mathbf{M} \phi_0^k = \begin{cases} 1 & l = k \\ 0 & \text{otherwise.} \end{cases} \quad (8)$$

The inner product \langle, \rangle is defined for the discretized system as a mass-weighted transpose multiplication. The mass weighting is used since all the mode shapes considered will be normalized with respect to Mass. This allows for the transformation of a vector of displacements $\hat{\mathbf{u}}$ to its modal projection η_0^k as

$$\eta_0^k = \phi_0^{kT} \mathbf{M} \hat{\mathbf{u}}. \quad (9)$$

In studying the k th mode, all of the weighting coefficients η_0^i , $i \neq k$, are set to 0, leading to $u_L(t) = \eta_0^k \phi_0^k e^{j\omega_0^k t}$. The first and second derivatives of this solution are, $\dot{u}_L(t) = j\omega_0^k u_L(t)$ and $\ddot{u}_L(t) = -\omega_0^{k2} u_L(t)$. The velocity has no real component, (recall that it is 90° out of phase with the displacement and acceleration for un-damped oscillations). This can be used to neglect the viscous terms in Eq. (5) when considering only the modal displacement.

Retaining the displacement as an unknown, substituting the velocity and acceleration in the original nonlinear equation (Eq. (5)), and setting the extant forcing term $f(t)$ to zero yields the quasi-static modal form for the k^{th} mode,

$$\mathbf{K} \mathbf{u}_k + F_{NL}(\mathbf{u}_k, \dot{\mathbf{u}}_k, \dots) = \alpha \mathbf{M} \phi_0^k. \quad (10)$$

The constant product $\omega_0^{k2} \eta_0^k$ is lumped into the modal forcing amplitude α . The subscript of u denotes the mode at which it is being excited. As α is varied from zero to a positive value, Eq. (10) represents the quasi-static loading of the system in the “shape” of its k th mode-shape over a range of modal amplitudes. The solution u is then transformed into the modal-space to obtain the contributions of any l^{th} mode of the system. In short, the modal forcing and displacement may be given as

$$\begin{aligned} F_k^l &= \alpha \left[\phi_0^{lT} \mathbf{M} \phi_0^k \right] = \begin{cases} \alpha & , l = k \\ 0 & , l \neq k \end{cases} \\ u_k^l &= \phi_0^{lT} \mathbf{M} \hat{\mathbf{u}}_k, \end{aligned} \quad (11)$$

where F_k^l and u_k^l denote the contribution of the l th mode on the quasi-static force and deformation of a system excited at its k th mode. Usually, u_k^k will be the greatest component in this. Using this in addition to the Masing conditions, it is possible to construct the hysteretic backbone curve for the friction model and thus calculate the natural frequency and damping factors of the nonlinear system at forcing level α . The subscripts 0 indicates that these calculations are based on the linearized low-amplitude (“stuck” interface) modes.

4.3. Friction models

Four friction models are considered for the current study: the single Jenkins element, a distributed four-parameter Iwan Model [49], a distributed five-parameter Iwan model [53], and a “middle-stuck” four-parameter Iwan Model. All of these may be classified as Masing models [9], which stipulate that for a steady-state response,

- The forward part of the hysteresis curve is identical to the reverse part of the hysteresis curve, only stretched by a factor of two and reflected across the axes when oscillating between two extremes.

- The equation of any hysteretic response curve is determined from the last point of the loading cycle before reversal and requiring that if the loading curve crosses a previous loading curve, it must correspond to the previous loading curve.

The above are often termed as Masing’s conditions and offer an effective way of relating the hysteretic backbone to the hysteresis loop. This is an essential requirement for the current approach since QSMA models just the backbone curve.

Fig. 5a depicts an illustrative hysteresis curve for a generic Masing model with a backbone $f(u)$ (with displacement u). The loading and unloading curves $f_l(u)$ and $f_u(u)$ are related via

$$\begin{aligned} f_l(u) &= -f_0 + 2f\left(\frac{u_0+u}{2}\right) \\ f_u(u) &= +f_0 - 2f\left(\frac{u_0-u}{2}\right). \end{aligned} \tag{12}$$

The energy dissipated per unit cycle (along the hysteresis curve at steady state) is given as the cyclic integral of the hysteresis path, i.e., the area under the hysteresis loop in Fig. 5a. It can be shown that

$$\begin{aligned} D(u_0) &= \oint_{-u_0}^{u_0} (f_l(u) - f_u(u)) du \\ &= -4f_0u_0 + 8 \int_0^{u_0} f(t) dt, \end{aligned} \tag{13}$$

where the integral term is the area under the backbone up to a displacement u_0 .

4.3.1. The Jenkins element

The single Jenkins model, whose backbone is depicted in Fig. 5b, is a linear spring connected serially to a frictional slider. The element behaves linearly until the spring force becomes equal to the threshold of the slider, after which it starts sliding with a constant force. Every pair of nodes connected with a Jenkins element is characterized by 2 parameters, the linear stiffness K_T , and the slipping force F_S . The forcing (backbone) and dissipation follow

$$f(u) = \begin{cases} K_T u, & K_T u < F_S \\ F_S, & K_T u \geq F_S, \text{ and} \end{cases} \tag{14}$$

$$\begin{aligned} D(u) &= -4F_S u + 8 \left(\frac{1}{2} \frac{F_S^2}{K_T} + F_S \left(u - \frac{F_S}{K_T} \right) \right) \quad (\text{if } K_T u \geq F_S) \\ &= \begin{cases} 0, & K_T u < F_S \\ 4F_S \left(u - \frac{F_S}{K_T} \right), & K_T u \geq F_S. \end{cases} \end{aligned} \tag{15}$$

Implementing Jenkins models with normal stiffness in three unique patches leads to a total of 9 parameters that must be estimated.

4.3.2. The four-parameter Iwan element

The Iwan class of models were originally introduced in the context of plasticity [31,30], but were later adapted for modeling frictional interactions[49]. The Iwan model is composed of a distribution of elementary Masing elements described by one or more continuously varied parameters. The integrated effect of these is then used to obtain a more detailed model.

The four-parameter Iwan model[49] is constructed using a parallel arrangement of Jenkins elements. After scaling the terms, the distributions are parameterized with the slider strengths ϕ . The reduced equations represent the force from a

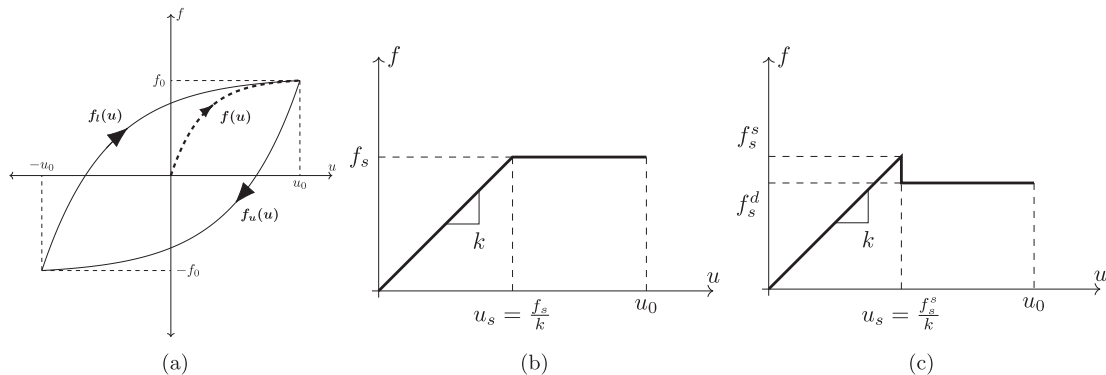


Fig. 5. Friction constitutive modeling that shows (a) an illustrative hysteresis curve of a Masing model, (b) a Jenkins model, and (c) a stiction Jenkins model backbone.

set of parallel Jenkins elements with unit stiffness and different slipping strengths. Here, $\rho(\phi)\delta\phi$ represents the count of elements with strength $\phi \in [\phi, \phi + \delta\phi)$. The distribution proposed in [49] was

$$\rho(\phi) = R\phi^\chi [H(\phi) - H(\phi - \phi_{\max})] + S\delta(\phi - \phi_{\max}), \tag{16}$$

where ϕ_{\max} represents the “macroslip strength”, $3 + \chi$ represents the power law slope of the dissipation, and R & S are mathematical constants. These four parameters completely describe the frictional interactions between a pair of points linked through the four-parameter Iwan element. The backbone and the cycle dissipation for the above four-parameter Iwan model is

$$f(u) = \begin{cases} \int_0^u \phi \rho(\phi) d\phi + u \int_u^{\phi_{\max}} \rho(\phi) d\phi, & u < \phi_{\max} \\ \int_0^{\phi_{\max}} \phi \rho(\phi) d\phi, & u \geq \phi_{\max} \end{cases} \tag{17}$$

$$= \begin{cases} \left(S + \frac{R\phi_{\max}^{\chi+1}}{\chi+1} \right) u - \frac{Ru^{\chi+2}}{(\chi+1)(\chi+2)}, & u < \phi_{\max} \\ \left(S + \frac{R\phi_{\max}^{\chi+1}}{\chi+2} \right) \phi_{\max}, & u \geq \phi_{\max}, \text{ and} \end{cases} \tag{18}$$

$$D(u) = \begin{cases} \int_0^u 4\phi(u - \phi)\rho(\phi) d\phi, & u < \phi_{\max} \\ \int_0^{\phi_{\max}} 4\phi(u - \phi)\rho(\phi) d\phi + 4S\phi_{\max}(u - \phi_{\max}), & u \geq \phi_{\max} \end{cases} \tag{19}$$

$$= \begin{cases} \frac{4Ru^{\chi+3}}{(\chi+2)(\chi+3)}, & u < \phi_{\max} \\ 4R\phi_{\max}^{\chi+2} \left(\frac{u}{\chi+2} - \frac{\phi_{\max}}{\chi+3} \right) + 4S\phi_{\max}(u - \phi_{\max}), & u \geq \phi_{\max}. \end{cases}$$

For the patch formulation, this will result in 15 parameters to be estimated.

4.3.3. The five-parameter Iwan element

In [53], a stick-slip formulation is introduced to the Iwan element by modifying the Jenkins element to include an additional parameter θ to model stiction by positing that the slipped element force is different from the slippage strength by a multiplicative factor

$$\theta = \frac{F_S^d}{F_S^s} \leq 1.0. \tag{20}$$

The superscripts d and s denote the dynamic (slipped) force and the static (strength) force respectively. An illustrative backbone is depicted for a single stiction Jenkins element in Fig. 5c. Using an identical treatment as for the four-parameter Iwan element, the backbone and cyclic dissipation is,

$$f(u) = \begin{cases} \int_0^u \theta\phi\rho(\phi) d\phi + u \int_u^{\phi_{\max}} \rho(\phi) d\phi, & u < \phi_{\max} \\ \int_0^{\phi_{\max}} \theta\phi\rho(\phi) d\phi, & u \geq \phi_{\max} \end{cases} \tag{21}$$

$$= \begin{cases} \left(S + \frac{R\phi_{\max}^{\chi+1}}{\chi+1} \right) u + Ru^{\chi+2} \left(\frac{\theta}{\chi+2} - \frac{1}{\chi+1} \right), & u < \phi_{\max} \\ \left(S + \frac{R\phi_{\max}^{\chi+1}}{\chi+2} \right) \theta\phi_{\max}, & u \geq \phi_{\max}, \text{ and} \end{cases}$$

$$D(u) = \begin{cases} \int_0^u 4\theta\phi(u - \frac{2\theta-1}{\theta}\phi)\rho(\phi) d\phi, & u < \phi_{\max} \\ \int_0^{\phi_{\max}} 4\theta\phi(u - \frac{2\theta-1}{\theta}\phi)\rho(\phi) d\phi + 4S\theta\phi_{\max}(u - \frac{2\theta-1}{\theta}\phi_{\max}), & u \geq \phi_{\max} \end{cases} \tag{22}$$

$$= \begin{cases} \frac{4Ru^{\chi+3}(\chi(1-\theta)+(2-\theta))}{(\chi+2)(\chi+3)}, & u < \phi_{\max} \\ 4R\theta\phi_{\max}^{\chi+2} \left(\frac{u}{\chi+2} - \frac{2\theta-1}{\theta} \frac{\phi_{\max}}{\chi+3} \right) + 4S\theta\phi_{\max}(u - \frac{2\theta-1}{\theta}\phi_{\max}), & u \geq \phi_{\max}. \end{cases}$$

The backbone expression has been previously derived in [53], but the dissipation expression is distinct from the published result due to the prior work not rigidly enforcing the Masing conditions. This leads to an 18 parameter estimation problem for the whole-joint modeled Brake-Reuß Beam interfaces.

Table 2

Summary of the contact models considered.

S.No.	Name	Number of Unknowns	Remarks
1.	Jenkins	$(2 + 1) \times 3 = 9$	Stick-Perfect slip elements
2.	Four-Parameter Iwan	$(4 + 1) \times 3 = 15$	Micro-slip elements
3.	Five-Parameter Iwan	$(5 + 1) \times 3 = 18$	Micro-slip elements with Stiction
4.	Middle-Stuck Four-Parameter Iwan	$(4 + 1) \times 2 + 2 = 12$	Micro-slip (+ fully stuck) elements

4.3.4. The middle-stuck four-parameter Iwan model

Since the innermost region in the interface (region 3 in Fig. 4a) is expected to have large normal force, this model uses linear springs in this region and the four-parameter Iwan models in the other four. Thus, this modeling approach will result in a total of 12 parameters that will have to be estimated.

Table 2 summarizes the four interfacial contact formulations considered for the current study. Strictly, the last formulation is not a fundamentally different contact model than formulation 2; it merely represents an exploration into the idea that the central patch may in fact always be in the “fully stuck” state, while accounting for the nonlinearity in the other patches.

4.3.5. Modal parameter estimation

Once a set of quasi-static simulations are conducted, the nonlinear natural frequency is estimated using the secant stiffness from the modal backbone (force-displacement curve)

$$\omega = \sqrt{\frac{f(u)}{u}}, \quad (23)$$

where u is the modal displacement amplitude, and $f(\cdot)$ is the backbone (u_k^k and α respectively, as per previous notation). The total dissipation D_{Total} is expressed as a sum of the dissipation across each of the nonlinear elements in the structure, D_i , added to the dissipation due to the underlying viscous damping factor ζ (estimated from low amplitude tests)

$$D_{Total} = \sum_{n=1}^{N_e} D_i(u) + 2\pi u^2 \omega^2 \zeta, \quad (24)$$

The factor $2\pi u^2 \omega^2$ comes from linear vibration theory (see any standard text like [52]), where the damping factor per cycle for a forced damped linear harmonic oscillator is

$$\zeta_n = \frac{D}{2\pi\omega\omega_n u^2}, \quad (25)$$

with ω and ω_n denoting the forced and natural frequencies respectively. Since the QSMA framework is equivalent to exciting the system at its natural frequency, the subscripts are dropped, leading to the corresponding term in Eq. (24). Following this, Eq. (25) is used to obtain the total equivalent damping factor for the system.

4.4. Pareto optimization

An important difference between previous attempts at characterizing joints using design exploration and the current work is in the objectives of the optimization problem. Where previous works such as [35] have weighted the frequency and damping deviations to obtain a single objective formulation, the present work retains the two as independent objectives.

An important idea in multi objective optimization is the concept of dominance of solutions. A set of solutions are said to be non-dominated if no solution in the set performs better than any other solution in the set in terms of *all* of the objectives [15]. This set, also commonly referred to as a Pareto set/front, lies in a space one rank below the objective-space (or error-space), eg., for a bi-objective problem, the Pareto front is a curve (1D), for a tri-objective problem it's a surface (2D), etc. Problems with a single point in the Pareto set imply that the objectives need not be treated independently and that optimizing one is sufficient to optimize the other. In most scenarios, however, this is not the case and the Pareto set consists of multiple solutions (or “designs”). Although weighing the objectives is a classical method for obtaining a unique optimizer for the problem, the choice of the weights is directly related to the portion of the Pareto set that will be highlighted. Another important issue is diversity in the population of both the design- as well as the error-space. Although the Pareto front may look sufficiently distributed in the error-space, the designs may be biased in the design-space. This issue gets more pronounced with larger design variables (see discussions on the “curse of dimensionality”, [47]).

Although significant advances have been made in evolutionary algorithms for MOOPs [16], unbiased design space population is a persisting issue in the community. The current investigation populates the design-space using a latin hypercube (LHS) based random sampling and evaluates the performance of each design before determining the correct designs. From [18] it can be inferred that as the dimension of the design-space increases, the number of data points to obtain an unbiased sampling of the whole domain increases geometrically. Thus design exploration becomes more difficult as the number of parameters to estimate increases.

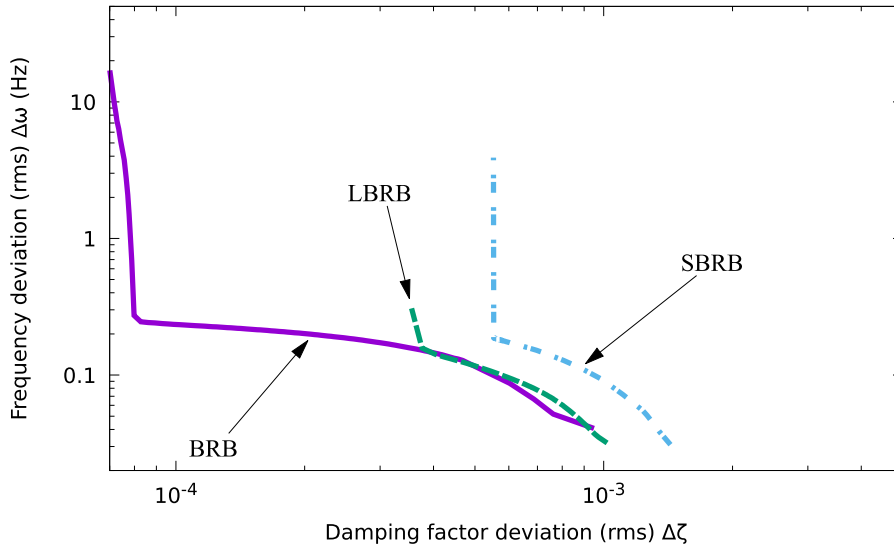


Fig. 6. Pareto fronts for four-parameter Iwan models modeling the interfaces of the three BRB configurations shown in Fig. 1.

Fig. 6 depicts the NSGA-II (Non-dominated Sorting Genetic Algorithm II [16]) populated Pareto fronts in terms of the root-mean-squared errors for the three beams with interfaces modeled using the four-parameter Iwan models. A hard minimum can be observed in the damping factor for all of the beams, with the magnitude of the minimum larger for the LBRB and the SBRB. This is because the damping factor predictions can only get as accurate as the low amplitude damping factor estimate is. Since there are no analytic methods of estimating the viscous damping factor, the low amplitude value from the BRB tests is used. The corresponding numbers for the other two beams show deviations within the same order of magnitude. Another important feature is the shape of the Pareto fronts—for a minimization problem, these are termed as non-convex fronts, which indicates the insufficiency of the model in matching the experimental frequency and dissipation observations. In other words, the Pareto front is interpreted as a metric for evaluating the epistemic uncertainty inherent to the modeling framework. For example, presence of prestress was observed to greatly influence the shape of the Pareto front (see Section 5.2.1). It is hypothesized that as the sources of epistemic uncertainty are removed from the model, the two response parameters will cease to be independent of each other, and the Pareto front will shrink to a single optimal design. That is, as the model form error is reduced, the area under the Pareto front will be reduced. As an example of this, in Section 5.2, the Pareto fronts calculated with the four-parameter Iwan model are consistently closer to the origin than those calculated with Jenkins elements for all three systems studied. This certainly indicates that there is some improvement in using the Iwan elements over the single Jenkins elements for whole joint simulations.

4.4.1. Methodology

Using the three-patch formulation (in which the parameters for pairs of patches 1 and 5 and 2 and 4 are taken as identical by symmetry), the Jenkins, middle-stuck 4-parameter Iwan, 4-parameter Iwan, and 5-parameter Iwan element approaches lead to 9, 12, 15, and 18 parameter formulations for the MOOP as previously noted. All of the current studies are performed by initializing these spaces with 5×10^6 LHS design points. Designs performing with a maximal error in frequency of 2 Hz (approximately half the maximum deviation in the BRB) and in damping factor of 5×10^{-3} (half an order of magnitude of the linear damping factor) are deemed as successful in fitting the current set of experimental data.

The maximal deviation may be formalized as the L_∞ deviation, which is defined as

$$L_\infty(q) = \max_i |q_i^{\text{model}} - q_i^{\text{expt}}|, \quad (26)$$

where q denotes a set of parameter predictions compared against the experiment and the superscripts identify the experiment and the model. For the current application, q is one of frequency or damping factor. Defining the tolerance level ϵ as above, the success criterion is written as

$$L_\infty(q) \leq \epsilon. \quad (27)$$

The L_∞ metric is chosen here since the specification of the maximum deviation bound can arise naturally from the desired accuracy in an application. This is equivalent to drawing a rectangle in the error space and selecting the designs that fall within its bounds. Calling this subspace of the selected designs as the acceptance region, an ideal surrogate system must have an acceptance region falling entirely within the acceptance region of its corresponding real structure. Any less than ideal surrogate system may be characterized by the relative size of the intersection of the two acceptance regions. This char-

acterization, referred henceforth as the *confidence of surrogacy*, is numerically estimated as the fraction of the number of designs in the acceptance region (from the random sampling) of the surrogate system that also lie in the acceptance region of the real system. The method, while not unbiased, will be used as a first estimate to assess the surrogate system hypothesis.

Representing the unknown parameters as $X \in \mathcal{R}^n$, and using $\mathcal{M}^I \subseteq \mathcal{R}^n$ to represent the acceptance region for beam I in the parameter space, the above definition for the surrogacy coefficient between beams I & J may be written as

$$SC_{IJ} = E \left[P \left(\underbrace{X \in \mathcal{M}^I}_{\mathcal{A}^I} \mid \underbrace{X \in \mathcal{M}^I}_{\mathcal{A}^I} \right) \right] = P(\mathcal{A}^I \mid \mathcal{A}^I). \tag{28}$$

Since all the calculations in the current work are conducted using random populations, the estimator for the metric \widehat{SC}_{IJ} is given by the estimator for the expectation of the event \mathcal{A}^I conditional to the event \mathcal{A}^I . This is given by

$$\widehat{SC}_{IJ} = E \left[\frac{P(X \in \mathcal{M}^I \cap \mathcal{M}^I)}{P(X \in \mathcal{M}^I)} \right] \tag{29}$$

$$\approx \frac{\sum_n I^I(x_n) I^I(x_n)}{\sum_n I^I(x_n)}$$

with, $I^I(x_n) = \begin{cases} 1 & x_n \in \mathcal{M}^I \\ 0 & \text{otherwise} \end{cases}$.

5. Results

5.1. Prestress and linear analysis

Fig. 7a presents the contact pressure distribution on the interface of the BRB after the static prestress analysis is performed in ABAQUS. The interface is modeled using a frictionless “hard” contact model. A cross-sectional view of the stresses

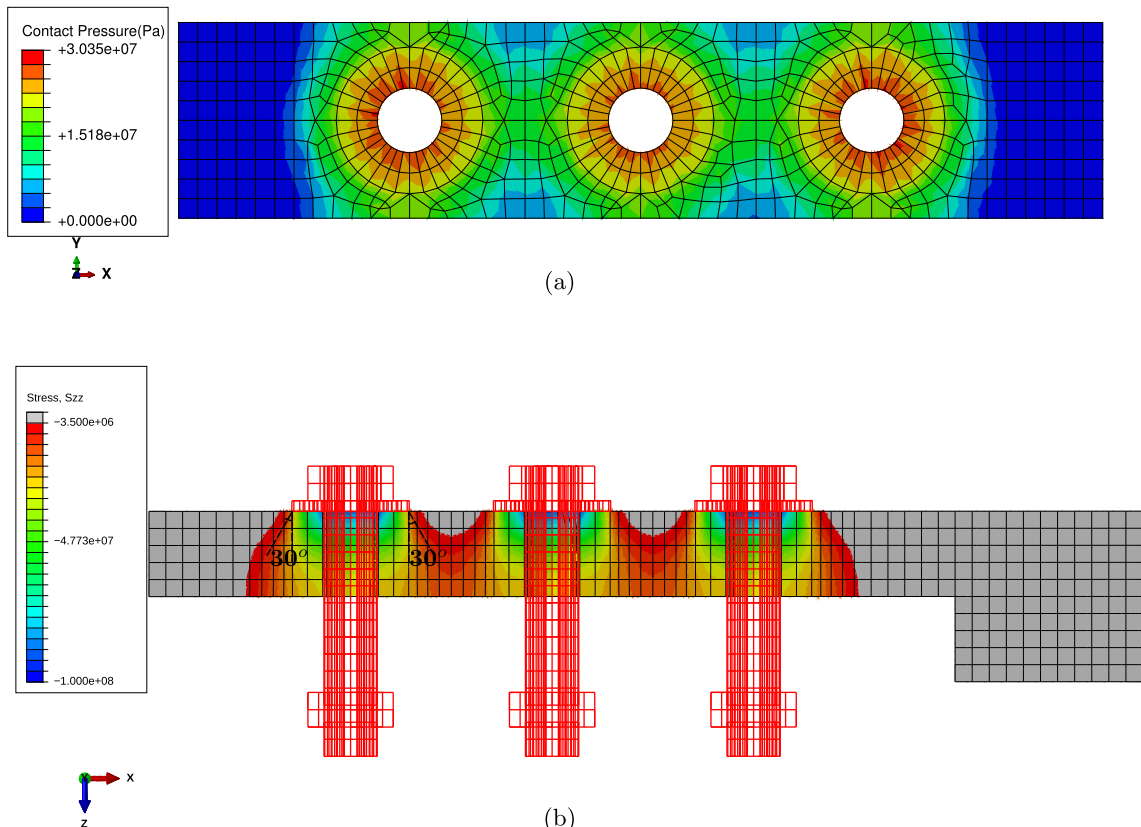


Fig. 7. Interface contact pressure of the BRB prestressed with a frictionless “hard” interface contact model: (a) surface normal, (b) Half beam cross-section.

developed is presented in Fig. 7b along with a reference frustum line of 30°. It can be seen that the angle approximately captures the cross-sectional pressure distribution.

From the simplified frustum idealization (see [10]), the normal directional member stiffness is

$$K_m = \frac{\pi E d \tan \alpha}{2} \log \left| \frac{(2t \tan \alpha + (D-d))(D+d)}{(2t \tan \alpha + (D+d))(D-d)} \right| \approx 7.5 \times 10^8 \text{ Nm}^{-1}. \quad (30)$$

The bolt stiffness, assuming a uniform cross section for the bolt, is approximated as,

$$K_b = \frac{A_b E}{l_b} \approx 3.7 \times 10^8 \text{ Nm}^{-1}. \quad (31)$$

In the above, the quantities E , d , D , t , A_b , l_b , and α are the Young's modulus (190×10^9 GPa), hole diameter (8.43 mm), washer diameter (17.46 mm), half-beam thickness (12.7 mm), bolt cross sectional area (49.5 mm^2), length of bolt in tension (25.4 mm), and frustum angle (30°). The total normal stiffness of each joint is approximately $K_b + K_m$ and comes out to be in the order of 10^9 N m^{-1} . While the above analysis is a coarse approximation, it helps narrow the bounds for parameter variation in the studies that follow. The normal directional stiffness is retained as a parameter to be estimated due to the high deviation expected from this approximation.

Fig. 8 presents the (scaled) first mode shape of the frequency analysis conducted on the prestressed system. It can be seen that the mode shapes of the BRB and the LBRB are qualitatively similar, but the SBRB appears to have a fundamentally different loading pattern in the joint-region. The current study is restricted to studying the results of the QSMA conducted on the depicted first bending mode over different amplitude ranges.

5.2. Nonlinear parameter estimation

Figs. 9–11 depict the performance of 5×10^6 LHS designs for the Jenkins, four-parameter Iwan, and the five-parameter Iwan models respectively. The middle-stuck formulation is not depicted since its characteristics are nearly identical to that of the four-parameter Iwan model. Table 3 summarizes the parameter limits used (as applicable) for each model. In each of the figures, the first column (figs. (a), (d), (g)) shows the error-space (using the maximum absolute deviations, or the L -infinity norms to define the space, $L_\infty[\omega] - L_\infty[\zeta]$) where, a box denoting the acceptance criterion is drawn over the design evaluations. Further, the performances of the Pareto front designs of all of the beams are connected by a line in each plot. While the Pareto designs of the SBRB are far outside of the acceptance region for the BRB and the LBRB, most of the designs from the Pareto fronts of the BRB and LBRB fall within the acceptance region for the SBRB. This hints at the presence of asymmetry in the concept of surrogacy, i.e., the BRB could be a good surrogate system for the SBRB while the SBRB may be a poor surrogate system for the BRB.

The second and third columns in the figures (figs. (b), (e), (h) and figs. (c), (f), (i)) show the actual response curves corresponding to three representative designs from the Pareto sets, which indicate a trade-off between predicting the frequency and the damping factor evolution. In the damping factor plots for the LBRB and the SBRB, there exists a minimum error in the

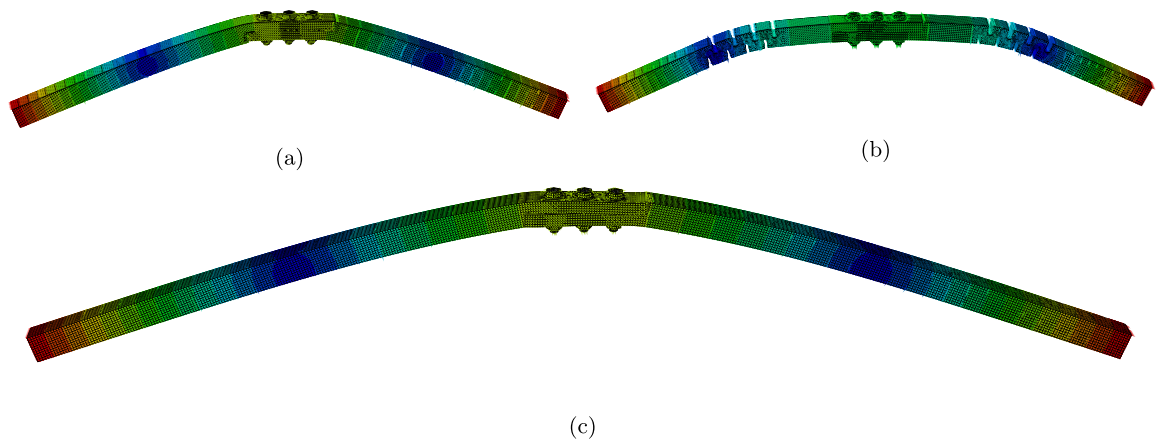


Fig. 8. Linear mode shapes of (a) the BRB, (b) the SBRB, and the (c) the LBRB (Contours colored by displacement magnitude). (For interpretation of the references to colour in this figure legend, the reader is referred to the web version of this article.)

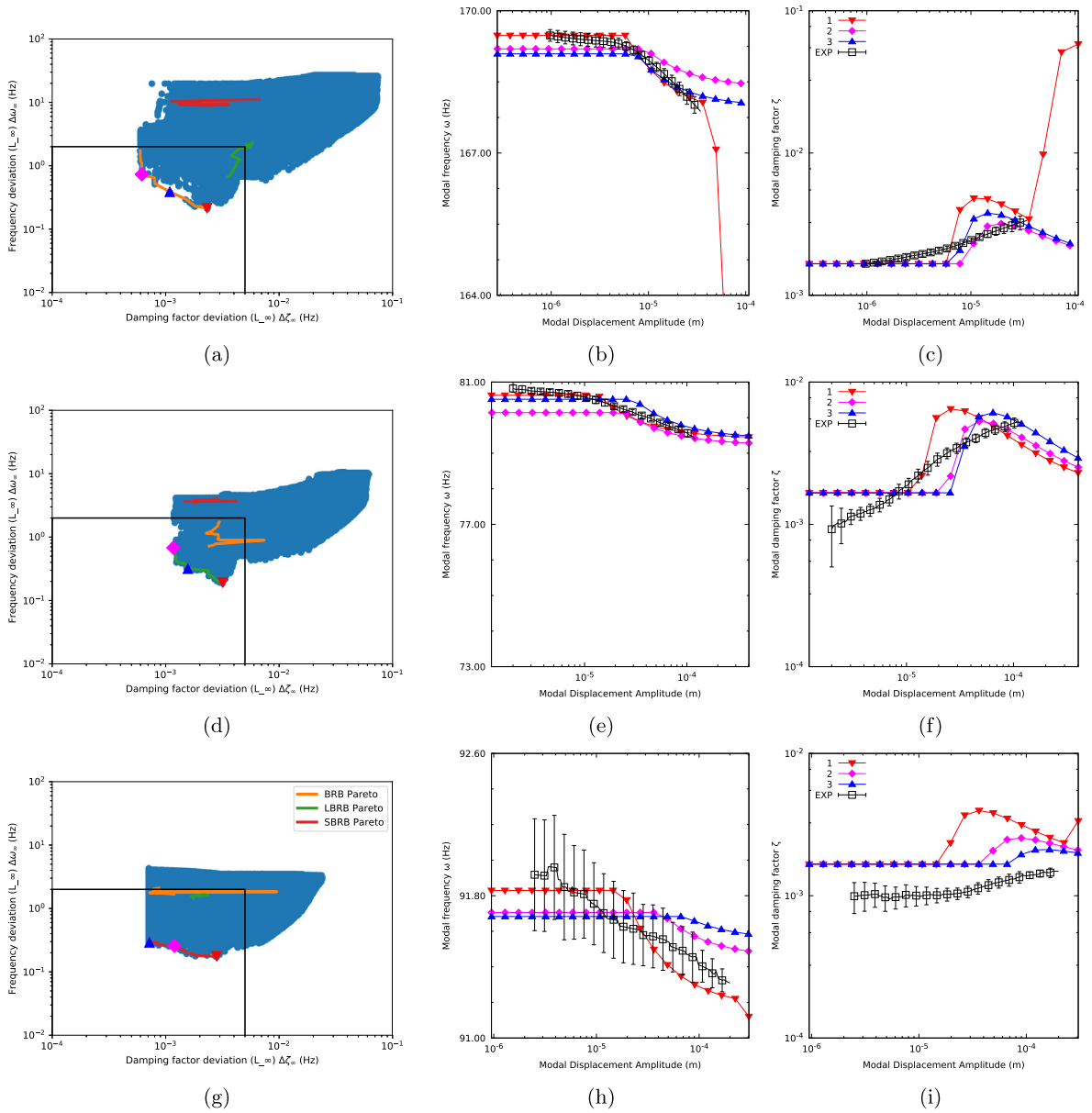


Fig. 9. Performance plots for the Jenkins model applied to the BRB ((a)–(c)), LBRB ((d)–(f)), & SBRB ((g)–(i)). Shown are the Pareto fronts ((a), (d), (g)) in the error space of $\Delta\omega_\infty$ & $\Delta\zeta_\infty$, and the modal amplitude dependence of ω ((b), (e), (h)) and ζ ((c), (f), (i)).

damping factors from the linear regime in all cases. This is due to using the damping factor of the nominal beam (BRB, see Table 1). The effect of using a different damping factor is explored at the end of the current section.

Since the Jenkins element consists of a “jump” between the stick and slip regimes, a non-smooth trend is present in the characteristic plots. The frequency and the damping factor are constant up to a critical displacement amplitude, after which they exhibit nonlinear effects. This can not be corroborated with physical observations and is a consequence of epistemic uncertainties characteristic to the Jenkins element. As previously noted, the location of the Pareto front is a strong qualitative indicator of the modeling uncertainty in the particular scenario. A closer inspection of the Pareto fronts in Figs. 9 and 10 is used to infer that the four-parameter Iwan element approach is more suitable than the Jenkins element approach for the current application. As expected, the response curves for the Iwan models are relatively smoother. It must be emphasized that the above issues with the Jenkins elements are due to the whole-joint-patched formulation and will be reduced/minimal in other contexts such as a node to node contact discretization.

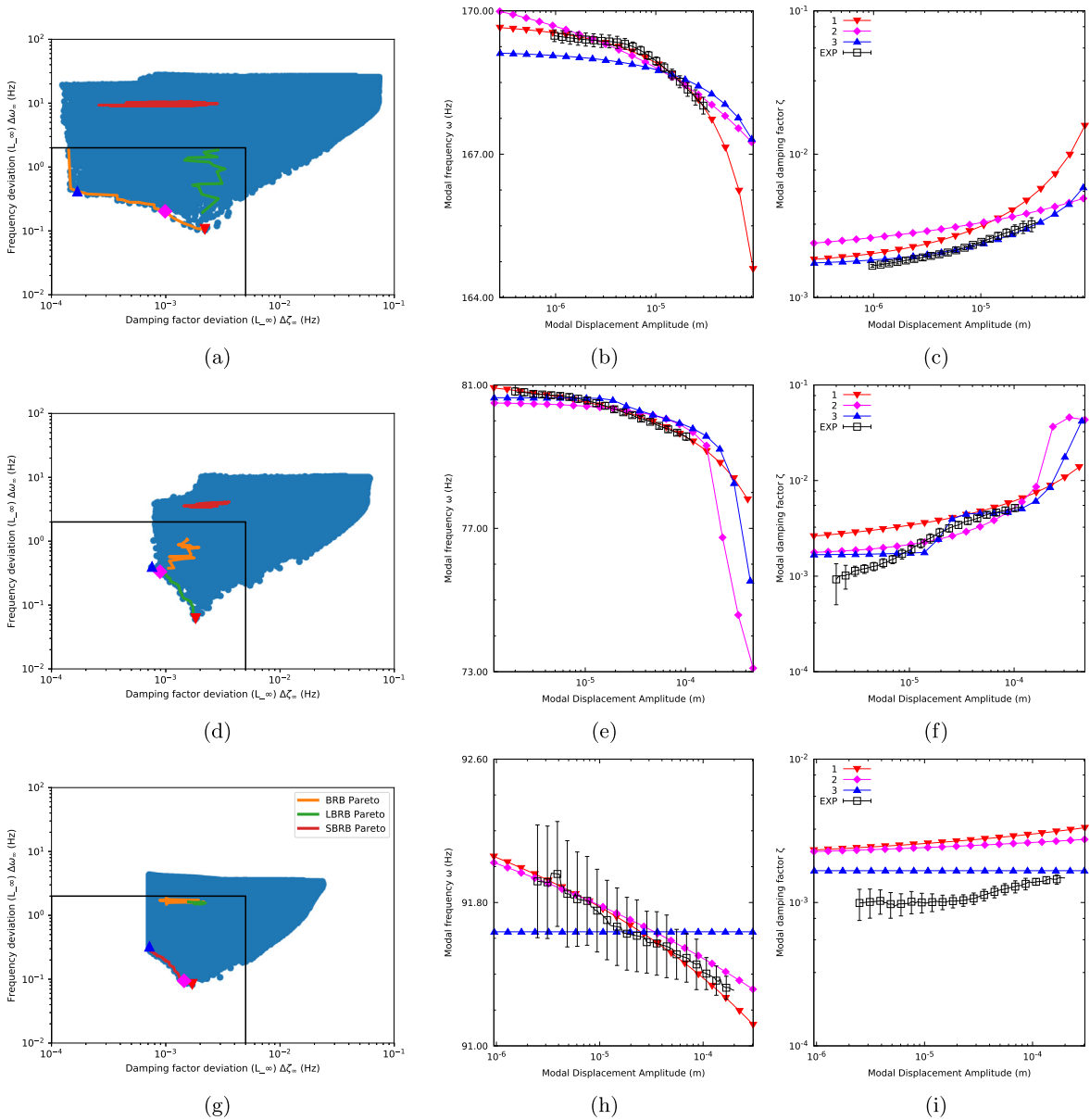


Fig. 10. Performance plots for the four-parameter Iwan model applied to the BRB ((a)–(c)), LBRB ((d)–(f)), & SBRB ((g)–(i)). Shown are the Pareto fronts ((a), (d), (g)) in the error space of $\Delta\omega_\infty$ & $\Delta\zeta_\infty$, and the modal amplitude dependence of ω ((b), (e), (h)) and ζ ((c), (f), (i)).

Table 4 shows three optimal design parameters (marked in Fig. 10) for the BRB simulated using the four-parameter Iwan models. The parameters do not show any signs of clustering; for instance, F_S values of region 2 are in the order of 10^9 N for the first and last designs but in the order of 10^2 N for the second. Further, the normal directional stiffness is off from the idealized estimate in Section 5.1 by as much as 3 orders of magnitude in the lower side and around 2 in the upper side. The challenges, as already noted, in conducting non-parametric parameter distribution studies are the issues with unbiased design population and the curse of dimensionality. Due to the lack of physicality of the parameters, coupled with the fact that the system never enters macroslip (which could give a better estimate of F_S), direct experimental estimation of the parameters is not straightforward.

5.2.1. The effect of prestress

In order to demonstrate the influence of the bolt prestress on the modeling uncertainties, Fig. 12 depicts the Pareto fronts for the SBRB modeled using the four-parameter Iwan models with and without the application of prestress. The no prestress

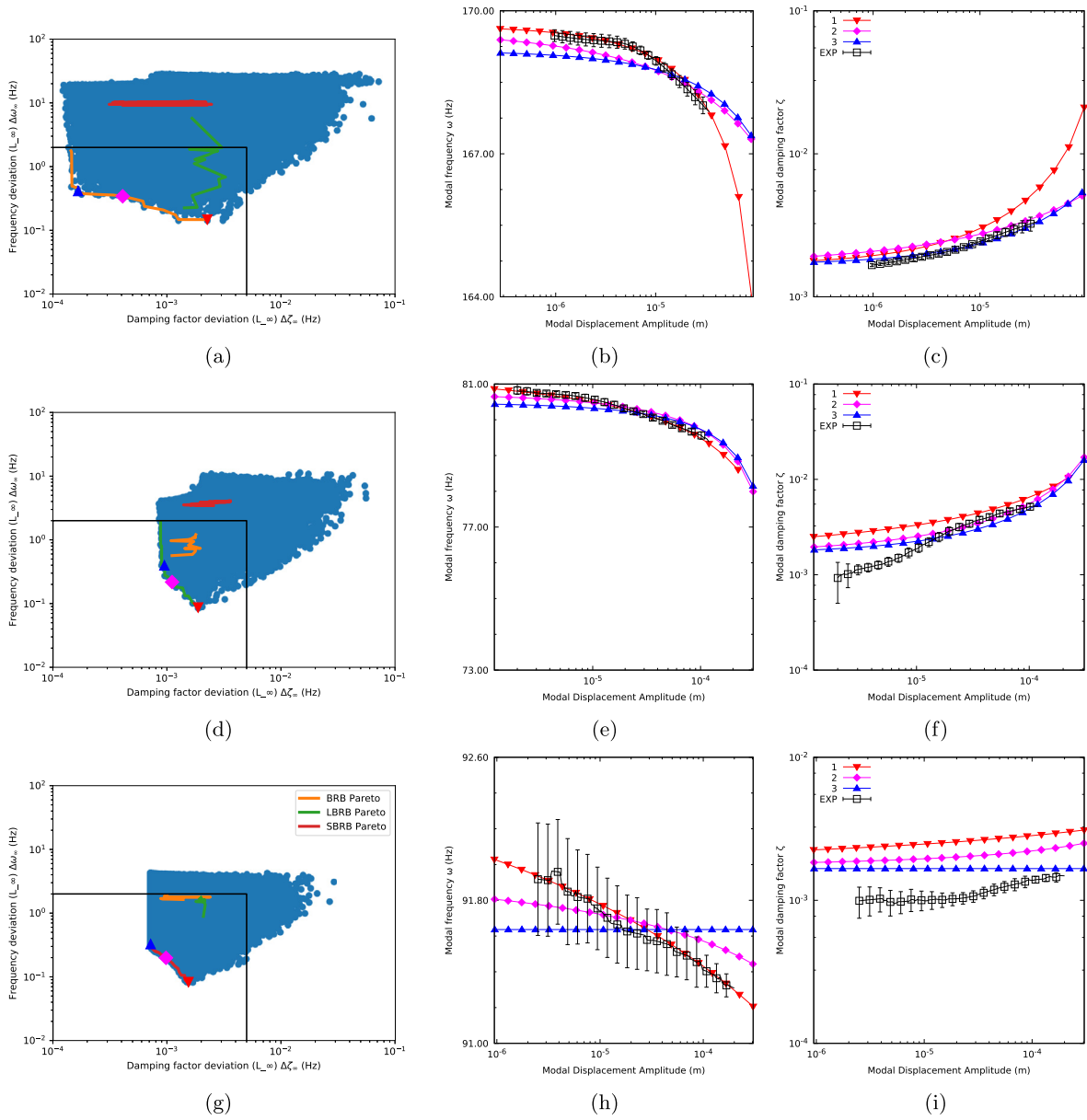


Fig. 11. Performance plots for the five-parameter Iwan model applied to the BRB ((a)–(c)), LBRB ((d)–(f)), & SBRB ((g)–(i)). Shown are the Pareto fronts ((a), (d), (g)) in the error space of $\Delta\omega_\infty$ & $\Delta\zeta_\infty$, and the modal amplitude dependence of ω ((b), (e), (h)) and ζ ((c), (f), (i)).

Table 3
Parameter limits for design exploration.

Parameter	Min.	Max.	Sampling
F_5	10^1 N	10^{11} N	Log-scale
K_T	10^2 N m ⁻¹	10^{14} N m ⁻¹	Log-scale
χ	-0.99	-0.01	Linear-scale
β	10^{-4}	10^4	Log-scale
θ	0.0	1.0	Linear-scale
K_Z	10^2 N m ⁻¹	10^{14} N m ⁻¹	Log-scale

Table 4

Illustrative optimal designs of the four-parameter Iwan Model for the BRB. Three rows per design denote interface regions 1, 2 & 3 respectively (as depicted in Fig. 4a).

Design ID.	F_S (N)	K_T (N m ⁻¹)	χ	β	K_z (N m ⁻¹)
1	4.4727×10^2	8.1842×10^8	-0.4854	1.4275×10^{-5}	1.0341×10^6
	5.9343×10^9	1.1501×10^7	-0.7244	1.4375×10^{-1}	1.2433×10^6
	3.0034×10^4	2.2452×10^6	-0.9682	1.0108×10^1	5.0676×10^5
2	5.2100×10^2	8.2470×10^8	-0.8623	7.2518×10^{-2}	1.0682×10^{10}
	7.3669×10^2	7.2860×10^{11}	-0.2776	7.7126×10^{-4}	8.5965×10^{10}
	1.2316×10^3	8.3824×10^5	-0.2244	3.0248×10^{-4}	4.3511×10^8
3	4.5916×10^2	7.3298×10^8	-0.4188	1.6614×10^0	3.4173×10^8
	2.0927×10^9	1.2864×10^5	-0.1401	1.0702×10^{-2}	3.5579×10^8
	1.3745×10^2	5.2988×10^2	-0.0636	2.4733×10^3	4.1171×10^9

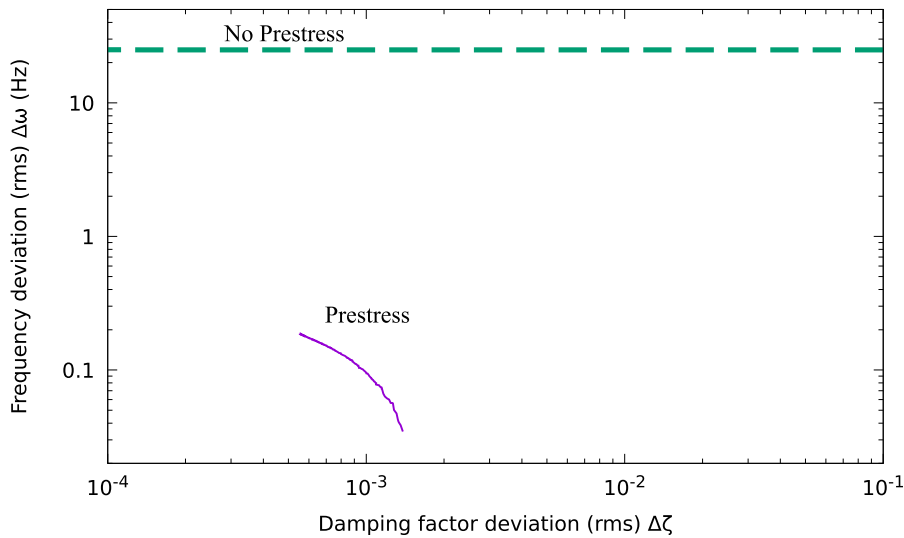


Fig. 12. The effect of prestress on the Pareto curve for the SBRB, with the interface modeled using four-parameter Iwan models.

model was created by skipping the initial static analysis step (detailed in Section 4.1) before the substructure generation. As a result, the matrices for this system correspond to a structure that does not include prestress augmentation (\mathbf{K}_A in Eq. (6)). Thus, this model is useful in highlighting the contribution of the prestress augmentation to the dynamic response of the structure.

It can be observed that it was not possible to tune the system for frequency deviations below around 25 Hz when the prestress is ignored. The prestressed system, on the other hand, shows that the models are capable of being tuned for frequency to a much lower deviation value. There are some other influences in the damping factor deviations too. This effect is observed to a lesser extent in the other beams, in terms of altering the Pareto fronts, but because of the nature of the loading (mode shape) of the SBRB, it is comparatively accentuated here. Therefore, subsequent modeling efforts should include the stiffness augmented due to prestress.

5.2.2. Confidence of surrogacy

In order to estimate the confidence of surrogacy of a “surrogate” system A with respect to a “real” system B, the accepted designs of system A are all used to model system B and their performances are recorded. Here, A and B could be any of the systems investigated. Selection is performed among this set (L_∞ criteria used here) and the ratio of the number of accepted designs to the total number of designs (accepted from system A) is calculated as the confidence of surrogacy.

Table 5 tabulates the surrogacy confidence estimates for the four friction models described previously. It must be noted that the low amplitude viscous damping factor used for all of the models here corresponds to the BRB (see Table 1). For the given three beams, nine distinct surrogate-real pairs are considered, giving rise to the matrix form of the tables. The rows

Table 5

Pairwise surrogacy confidence estimates for the (a) Jenkins, (b) 4-parameter Iwan, (c) 5-parameter Iwan, and (d) middle-stuck 4-parameter Iwan models with $\zeta_{lin} = 1665.9340 \times 10^{-6}$. S-Surrogate system, R-Real system.

(a)				(b)			
S \ R	BRB	LBRB	SBRB	S \ R	BRB	LBRB	SBRB
BRB	1.000000	0.985275	0.845466	BRB	1.000000	0.988733	0.860906
LBRB	0.348352	1.000000	0.773051	LBRB	0.353605	1.000000	0.779876
SBRB	0.050213	0.129858	1.000000	SBRB	0.052984	0.134206	1.000000

(c)				(d)			
S \ R	BRB	LBRB	SBRB	S \ R	BRB	LBRB	SBRB
BRB	1.000000	0.999133	0.865767	BRB	1.000000	0.988114	0.914896
LBRB	0.354764	1.000000	0.777457	LBRB	0.355002	1.000000	0.776607
SBRB	0.048816	0.122464	1.000000	SBRB	0.056319	0.133064	1.000000

denote the beam considered as the surrogate system and the columns denote the beam considered as the real system. Two immediate conclusions are apparent from the tabulation:

1. The estimates show greater sensitivity to the beam pair than the modeling approach.
2. Surrogacy is a one-way relationship, i.e., a non-commutative property.

The implication of the first property is that this shows that there is an inherent metric that can be estimated independent of how the system is modeled. With all of the uncertainties associated with friction constitutive modeling, it is not trivial to decide the most applicable one. The current results provide a metric that can be used to evaluate the ability of one structure to act as a “test-bed” for another. For example, the surrogacy confidence of the BRB for the LBRB is estimated as 99.03% (averaged over the four models). This implies that parameter estimates from experimental data of the BRB alone is 99.03% certain to model the LBRB to comparable accuracy. Thus, to make design decisions for the LBRB, the beam itself does not need to be tested if the confidence in the surrogacy of the BRB is deemed sufficient.

One ramification of the ability to quantify the confidence is that future design efforts could use a set of known joint models measured from well-suited surrogate systems to predict the response of a novel structure accurately, and to optimize a design with known confidence. Further, in applications where fabrication and testing of prototypes or design iterations is expensive and time consuming, this approach of modeling with parameters deduced from a surrogate structure should significantly reduce project costs and durations. It can be seen that while the BRB has the highest surrogacy confidence values with respect the other two beams, the corresponding values of the SBRB are significantly less. This indicates that by design, the SBRB is a poor choice for a surrogate structure while the BRB comes out to be the best one.

In order to study the dependence of these estimates on the different factors in each estimation process, an analysis of variance (ANOVA) test was set up posing the surrogate beams, the real beams, the friction model, and the linear damping ratio as four factors. The current study explores the three beams as the levels for the beam factors, the four friction models as the levels for the friction model factor, and the three linearized damping ratios (from Table 1) as the levels for the linearized damping ratio factor. Table 6 presents the results of the four-way ANOVA test. With over 97% confidence, the friction

Table 6

ANOVA Table (4-way) for surrogacy confidence.

Factor	Df	Sum Sq.	Mean Sq.	F value	Pr(>F)
Beam S	2	31.23	15.616	267.533	$< 2 \times 10^{-16}$
Beam R	2	56.80	28.399	486.523	$< 2 \times 10^{-16}$
Friction Model	3	0.01	0.005	0.081	0.971
Linearized ζ	2	0.00	0.000	0.000	1.000
Residuals	1070	62.46	0.058		

model and linear damping factor have no influence on the coefficient of surrogacy, The choice of system for the surrogate, though, is paramount for the coefficient of surrogacy (with a likelihood of being rejected $< 2 \times 10^{-16}\%$).

The second property is reflected in the asymmetry in the coefficients $SC_{AB} \neq SC_{BA}$ revealing that the surrogacy of one structure for another does not estimate the surrogacy in the opposite way. Therefore, a carefully designed surrogate structure could be made to have high surrogacy confidence for a wide range of real structures.

Upon inspection of the estimates in Table 5 and the response curves in Fig. 3 the fact that the LBRB has a surrogacy of only around 34% for the BRB while the BRB has more than a 98% surrogacy for the LBRB is somewhat surprising at first. The response of the LBRB seems to be different from that of the BRB since it appears to be operating at a much higher level of dissipation change than the BRB for each modal amplitude level. This suggests that the modal amplitude may not be the right parameterization for the response curves since the joint loading state for a given modal amplitude is not identical for different structures. A better parameterization should capture the expected loading on the interface more closely.

6. Discussions

Despite the fact that the contact modeling approach adopted in the current work is simplistic, it has been demonstrated that it is sufficient to make meaningful predictions for a bolted structure, provided the parameters may be tuned satisfactorily. The nature of the Pareto front is taken as an indicator of the “tunability” of a particular contact model to represent the response of a given structure, and the surrogacy estimate represents the applicability of the so-tuned parameters across different structures and/or loading cases.

An important factor in the adopted estimation procedure is the acceptance bounds placed in the error space—modifying this was seen to slowly perturb the confidence estimates until the properties break down. Thus, owing to the inherent modeling uncertainties, the existence of optimal error bounds is inferred to provide the most robust confidence estimates. As an extension of the current work, the surrogacy confidences between two modes of the same structure could be assessed, which will be useful to determine whether or not studying just a single mode will be sufficient to characterize the complete system (see [4] for preliminary results).

Besides this, one significant issue with using sophisticated constitutive models for modeling friction in jointed structures comes from the fact that most of these will be parametrized by non-physical mathematical constants. This makes the parameter identification problem more complicated leading to difficulties in interpreting empirical models. Posing this as an MOOP is shown to reveal important features of both the employed constitutive model as well as the structure it is used to model. As noted above, the Pareto front in the error-space is related to the efficacy of the model to describe the experimental observations. In addition to the model, many factors are believed to contribute to the structure to this end; the joint reduction approach, the solution methodology, etc. Although it is beyond the scope of the current work to assess the effects each of these has, the Pareto fronts provide a valuable method of understanding how appropriate a particular modeling approach is to make predictive models.

An important physical aspect is that the dynamics of an assembled system are expected to be dependent upon the normal contact force within the interfaces. In this study, however, normal force dependency was not directly investigated due to the limitations of the considered models. Moreover, by fixing the model parameters for each patch over the vibration cycle, it is assumed that the contact stresses do not change as the structure vibrates. There have, however, been experimental studies that demonstrably show that this assumption is incorrect (see, for example, [48]). The effect of prestress on the model estimation must be studied in further detail. Extending the approach to normal-force dependent friction models may require alternate simulation methods since these are no longer Masing models, which violates a requirement for QSMA. The available alternatives include transient simulations and frequency domain solvers. Using either of these, especially for the more sophisticated friction models, will result in very large computational times making design exploration in the current spirit prohibitively expensive. A slightly modified approach would be the quasi-static direct hysteretic modeling, wherein the full hysteresis curve is simulated quasi-statically. The system is taken through the backbone to the peak displacement, and quasi-statically unloaded and reloaded to trace the complete hysteresis loop. Demonstrated to be applicable for elastic dry friction models in [17] the authors are currently investigating the applicability of this approach to a general hysteretic constitutive law.

7. Conclusions

The paper has two major contributions: the definition & testing of a surrogate system hypothesis for jointed systems, and a numerical estimator for the developed metric.

This paper defines the surrogate system hypothesis as stating that the physical properties of a joint are identical irrespective of its structural context. The implications of this hypothesis could be in contrast with the whole joint modeling approach used commonly over the last two decades in which the properties of a joint are deduced as part of the structure, not as an isolated interface. In order to test this hypothesis, a quantitative metric has been defined so as to evaluate the applicability of experimental observations from one jointed structure to another. Estimates of these are shown to be relatively independent of the frictional models used to model the interfaces, and hence, the estimation of these constants provides a way of studying the structures under the purview of a design-space.

An estimate of the surrogacy metric is formulated and demonstrated to be applicable for a set of bolted lap-joint structures with identical interfaces. Going forward, however, it will be of relevance to come up with alternative and possibly cheaper approaches for the estimation. The suitability of evolutionary algorithms will have to be assessed more rigorously. Preliminary efforts showed that improper implementations may lead to random clustering in the design-space. This could lead to high biases in the confidence estimates and have very high dependence on the initial population.

In the absence of a better estimation strategy, the estimation process must be carried out for models with varying sophistication in terms of finer contact patches or better interface models. As already mentioned, an important drawback in scaling up the procedure to more patches/parameters is the computational overhead it incurs. As the parameter space grows (in dimensionality), the number of designs that will have to be sampled to span the entire space sufficiently will increase geometrically, making the outlined procedure ill-suited for the application. This can, however, be countered in part by employing more physical contact models, such as rough contact models (see [26], for instance) and implementing them in a traction-consistent formulation (such as the models presented in [17]), keeping the total number of unknowns to a small number, while preserving interfacial kinematics.

In assessing the surrogate system hypothesis for jointed structures, it can be concluded that it is possible to quantify and estimate the surrogacy potential of any structure to model any other structure using empirical design exploration. Further, this approach may have potential applications in other areas of nonlinear systems too.

Acknowledgements

The authors thank the participants of the Nonlinear Mechanics and Dynamics (NOMAD) Research Institute of 2016 for the experimental data and Robert M. Lacayo for helpful discussions. *Funding:* This material is based upon work supported by the National Science Foundation under Grant No. 1744327.

Appendix A. Engineering drawings

See Figs. 13–15.

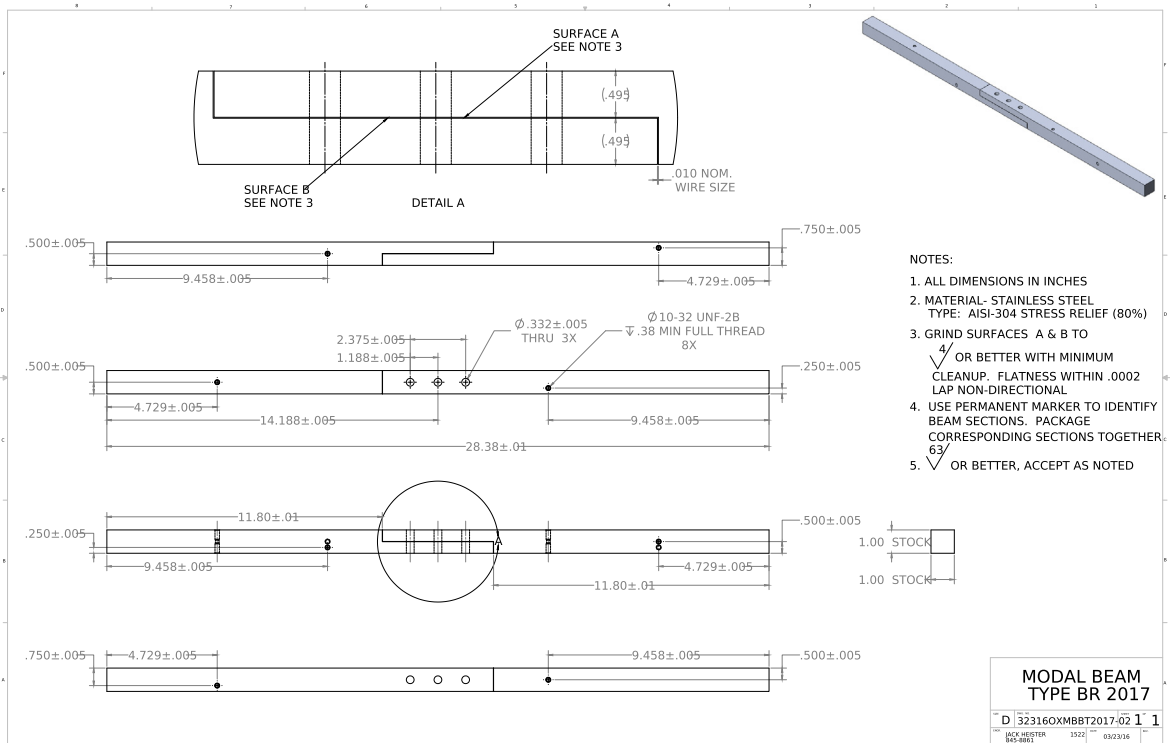


Fig. 13. Nominal Brake-Reuß beam (BRB).

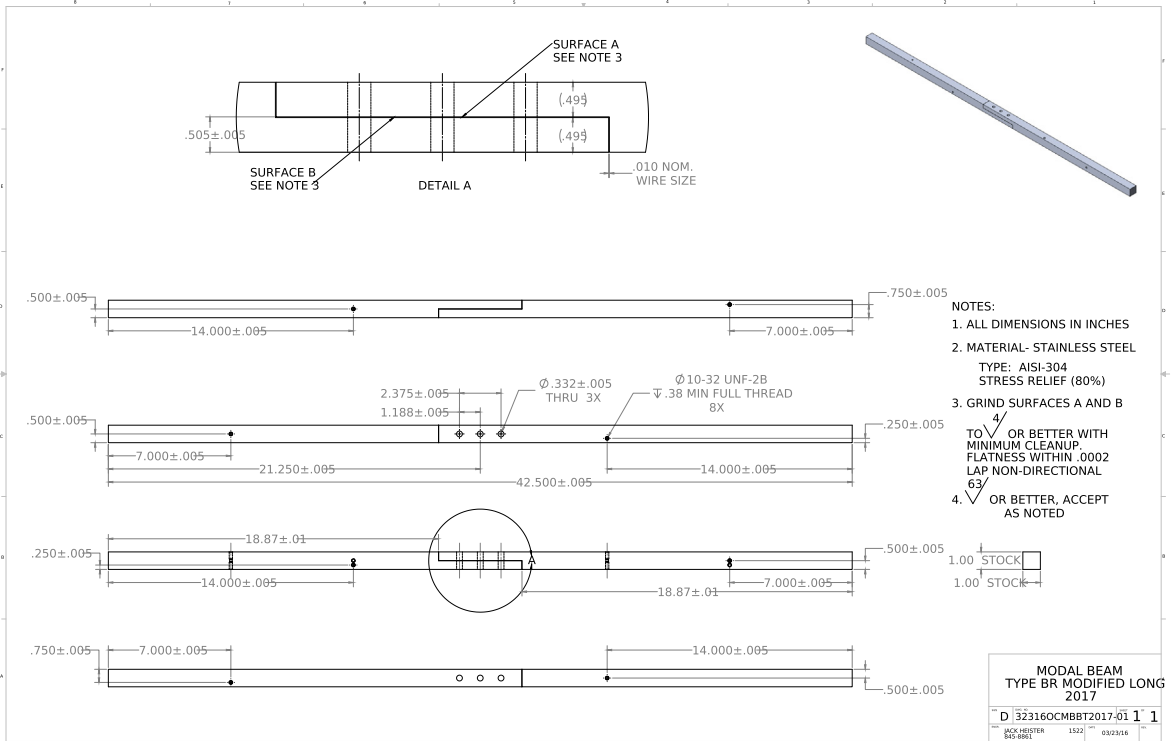


Fig. 14. Length-modified Brake-Reuß beam (LBRB).

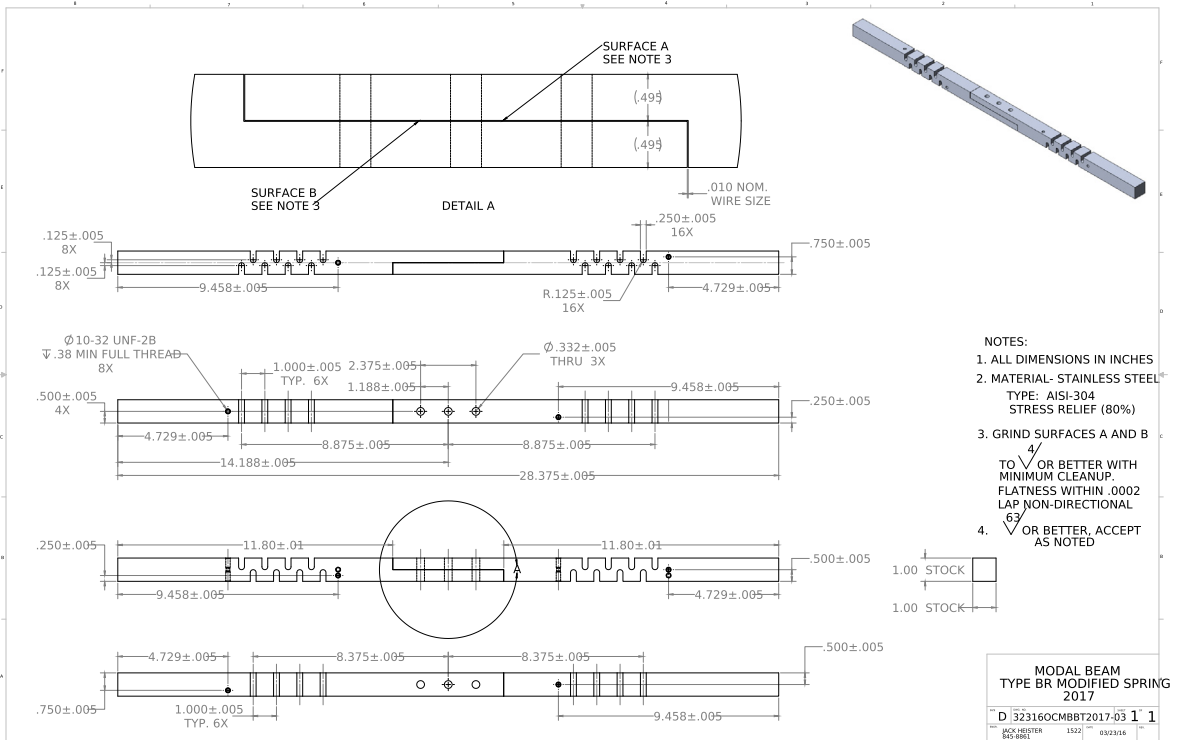


Fig. 15. Stiffness-modified Brake-Reuß beam (SBRB).

References

- [1] H. Ahmadian, H. Jalali, Identification of bolted lap joints parameters in assembled structures, *Mech. Syst. Signal Process.* 21 (2007) 1041–1050.
- [2] M.S. Allen, R.M. Lacayo, M.R.W. Brake, Quasi-static modal analysis based on implicit condensation for structures with nonlinear joints, in: *International Conference on Noise and Vibration Engineering*, Leuven, Belgium, 2016.
- [3] J. Armand, L. Salles, C.W. Schwingshackl, D. Süß, K. Willner, On the effects of roughness on the nonlinear dynamics of a bolted joint: a multiscale analysis, *Eur. J. Mech.-A/Solids* 70 (2018) 44–57.
- [4] N.N. Balaji, M.R.W. Brake, On the modal surrogacy of joint parameter estimates in bolted joints, in: *37th International Modal Analysis Conference (IMAC XXXVII)*, Orlando, FL, 2019.
- [5] A. Bindemann, A.A. Ferri, The influence of friction models on passive damping and dynamic response of a flexible beam structure, in: *36th Structures, Structural Dynamics and Materials Conference*, American Institute of Aeronautics and Astronautics, 1995, <https://doi.org/10.2514/6.1995-1178>.
- [6] S. Bograd, P. Reuß, A. Schmidt, L. Gaul, M. Mayer, Modeling the dynamics of mechanical joints, *Mech. Syst. Signal Process.* 25 (2011) 2801–2826.
- [7] M.R.W. Brake, C.R. Little, A.R. Lewis, M.T. O’Gorman, Reconciling whole joint models and the preservation of local kinematics, in: *International Design Engineering Technical Conference*, ASME, Cleveland, OH, 2017.
- [8] M.R.W. Brake, C.W. Schwingshackl, P. Reuß, On the observed variability and repeatability in jointed structures, *Mech. Syst. Signal Process.* (under review).
- [9] M.R.W. Brake, An overview of constitutive models, in: *The Mechanics of Jointed Structures*, Springer, 2018, pp. 207–221.
- [10] R.G. Budynas, K. Nisbett, *Shigley’s Mechanical Engineering Design*, 10th ed., McGraw Hill, 2014.
- [11] A. Cabbai, T. Putelat, J. Woodhouse, The frequency response of dynamic friction: enhanced rate-and-state models, *J. Mech. Phys. Solids* 92 (2016) 210–236.
- [12] R.D. Cook, D.S. Malkus, M.E. Plesha, R.J. Witt, *Concepts and Applications of Finite Element Analysis*, John Wiley and Sons, 2002.
- [13] S.B. Cooper, M. Rosatello, A. Mathis, K. Johnson, M.R.W. Brake, M.S. Allen, A.A. Ferri, D.R. Roettgen, B.R. Pacini, R.L. Mayes, Effect of far-field structure on joint properties, in: *35th International Modal Analysis Conference (IMAC XXXV)*, Garden Grove, CA, 2017.
- [14] R.R. Craig, M.C.C. Bampton, Coupling of substructures for dynamic analyses, *AIAA J.* 6 (7) (1968) 1313–1319.
- [15] K. Deb, *Multi-objective Optimization using Evolutionary Algorithms*, vol. 16, John Wiley & Sons, 2001.
- [16] K. Deb, A. Pratap, S. Agarwal, T. Meyarivan, A fast and elitist multiobjective genetic algorithm: NSGA-II, *IEEE Trans. Evol. Comput.* 6 (2) (2002) 182–197.
- [17] T. Dreher, N.N. Balaji, J. Groß, M.R.W. Brake, M. Krack, Gerrymandering for interfaces: modeling the mechanics of jointed structures, in: *37th International Modal Analysis Conference (IMAC XXXVII)*, Orlando, FL, 2019.
- [18] V. Epanechnikov, Non-parametric estimation of a multivariate probability density, *Theory Prob. Appl.* 14 (1) (1969) 153–158, <https://doi.org/10.1137/1114019>, ISSN 0040-585X.
- [19] M. Eriten, A.A. Polycarpou, L.A. Bergman, Surface roughness effects on energy dissipation in fretting contact of nominally flat surfaces, *ASME J. Appl. Mech.* 78 (2011), Art. 021011.
- [20] M. Eriten, A.A. Polycarpou, L.A. Bergman, Physics-based modeling for fretting behavior of nominally flat rough surfaces, *Int. J. Solids Struct.* 48 (2011) 1436–1450.
- [21] D.J. Ewins, A survey of contact hysteresis measurement techniques, in: *The Mechanics of Jointed Structures*, Springer, 2018, pp. 149–179.
- [22] M. Feldman, Non-linear system vibration analysis using Hilbert transform – i. Free vibration analysis method ‘Freevib’, *Mech. Syst. Signal Process.* 8 (1994) 119–127.
- [23] H. Festjens, G. Chevallier, J.-L. Dion, A numerical tool for the design of assembled structures under dynamic loads, *Int. J. Mech. Sci.* 75 (2013) 170–177.
- [24] C. Gastaldi, A. Fantetti, T. Berruti, Forced response prediction of turbine blades with flexible dampers: the impact of engineering modelling choices, *Appl. Sci.* 8 (1) (2017) 34, <https://doi.org/10.3390/app8010034>, ISSN 2076-3417.
- [25] L. Gaul, R. Nitsche, The role of friction in mechanical joints, *ASME Appl. Mech. Rev.* 54 (2001) 93–110.
- [26] J.A. Greenwood, J.B.P. Williamson, Contact of nominally flat surfaces, *Proc. R. Soc. London Ser. A* 295 (1966) 300–319.
- [27] Z. Guo, M.R.W. Brake, M.S. Bonney, Uncertainty quantification considerations of friction model parameters for joint mechanics applications, *J. Sound Vib.* (under review).
- [28] J.J. Hollkamp, R.W. Gordon, Reduced-order models for nonlinear response prediction: implicit condensation and expansion, *J. Sound Vib.* 318 (4–5) (2008) 1139–1153.
- [29] W.C. Hurty, Dynamic analysis of structural systems using component modes, *AIAA J.* 3 (1960) 678–685.
- [30] W.D. Iwan, A distributed-element model for hysteresis and its steady state dynamic response, *ASME J. Appl. Mech.* 33 (1966) 893–900.
- [31] W.D. Iwan, On a class of models for the yielding behavior of continuous and composite systems, *ASME J. Appl. Mech.* 34 (1967) 612–617.
- [32] G. Kerschen, K. Worden, A.F. Vakakis, J.C. Golinval, Past, present and future of nonlinear system identification in structural dynamics, *Mech. Syst. Signal Process.* 20 (2006) 505–592.
- [33] G. Kerschen, K. Worden, A.F. Vakakis, J.-C. Golinval, Nonlinear system identification in structural dynamics: current status and future directions, in: *25th International Modal Analysis Conference (IMAC XXV)*, Orlando, FL, 2007.
- [34] D. Krattiger, L. Wu, M. Zacharczuk, M. Buck, R.J. Kuether, M.S. Allen, P. Tiso, M.R.W. Brake, Interface reduction for hurty/craig-bampton substructured models: review and improvements, *Mech. Syst. Signal Process.* 114 (2019) 579–603, <https://doi.org/10.1016/j.ymssp.2018.05.031>, ISSN 0888-3270.
- [35] R.J. Kuether, D.A. Najera, Parameter estimation of joint models using global optimization, in: *Dynamics of Coupled Structures*, Springer, 2017, pp. 29–39, vol. 4.
- [36] R. Lacayo, L. Pesaresi, J. Groß, D. Fochler, J. Armand, L. Salles, C.W. Schwingshackl, M. Allen, M. Brake, Nonlinear modeling of structures with bolted joints: a comparison of two approaches based on a time-domain and frequency-domain solver, *Mech. Syst. Signal Process.* 114 (2019) 413–438, <https://doi.org/10.1016/j.ymssp.2018.05.033>, ISSN 0888-3270.
- [37] R.M. Lacayo, M.S. Allen, Updating structural models containing nonlinear Iwan joints using quasi-static modal analysis, *Mech. Syst. Signal Process.* 118 (2019) 133–157, <https://doi.org/10.1016/j.ymssp.2018.08.034>, ISSN 08883270.
- [38] S. Nacivet, C. Pierre, F. Thouverez, L. Jezequel, A dynamic lagrangian frequency-time method for the vibration of dry-friction-damped systems, *J. Sound Vib.* 265 (1) (2003) 201–219.
- [39] J.P. Noël, G. Kerschen, Nonlinear system identification in structural dynamics: 10 more years of progress, *Mech. Syst. Signal Process.* 83 (2017) 2–35, <https://doi.org/10.1016/j.ymssp.2016.07.02>, ISSN 0888-3270.
- [40] L. Pesaresi, J. Armand, C.W. Schwingshackl, L. Salles, C. Wong, An advanced underplatform damper modelling approach based on a microslip contact model, *J. Sound Vib.* (2018), <https://doi.org/10.1016/j.jsv.2018.08.014>, ISSN 0022-460X.
- [41] E.P. Petrov, D.J. Ewins, Analytical formulation of friction interface elements for analysis of nonlinear multi-harmonic vibrations of bladed disks, *J. Turbomach.* 125 (2) (2003) 364, <https://doi.org/10.1115/1.1539868>, ISSN 0889504X.
- [42] A.S. Phani, S. Adhikari, Rayleigh quotient and dissipative systems, *J. Appl. Mech.* 75 (6) (2008), <https://doi.org/10.1115/1.2910898>, 061005-061005-6, ISSN 0021-8936.
- [43] F. Pichler, W. Witteveen, W. P. Fischer, Reduced-order modeling of preloaded bolted structures in multibody systems by the use of trial vector derivatives, *J. Comput. Nonlinear Dyn.* 12 (5) (2017) 051032–051032-12, <https://doi.org/10.1115/1.4036989>, ISSN 1555-1415.
- [44] K.Y. Sanliturk, D.J. Ewins, Modelling two-dimensional friction contact and its application using harmonic balance method, *J. Sound Vib.* 193 (1996) 511–523.
- [45] C.W. Schwingshackl, Measurement of friction contact parameters for nonlinear dynamic analysis, in: *30th International Modal Analysis Conference (IMAC XXX)*, Jacksonville, FL, 2012.

- [46] C.W. Schwingshackl, E.P. Petrov, D.J. Ewins, Measured and estimated friction interface parameters in a nonlinear dynamic analysis, *Mech. Syst. Signal Process.* 28 (2012) 574–584.
- [47] D.W. Scott, *Multivariate Density Estimation: Theory, Practice, and Visualization*, John Wiley & Sons, 2015.
- [48] B. Seeger, P. Butaud, F. Du, V. Baloglu, M.R.W. Brake, C.W. Schwingshackl, In situ measurements of interfacial contact pressure during impact hammer tests, in: *36th International Modal Analysis Conference (IMAC XXXVI)*, Orlando, FL, 2018.
- [49] D.J. Segalman, A four-parameter Iwan model for lap-type joints, *J. Appl. Mech.* 72 (5) (2005) 752–760.
- [50] D.J. Segalman, D.L. Gregory, M.J. Starr, B.R. Resor, M.D. Jew, J.P. Lauffer, N.M. Ames, *Handbook on Dynamics of Jointed Structures Technical Report SAND2009-4164*, Sandia National Laboratories, Albuquerque, NM, 2009.
- [51] J.W. Strutt, *The Theory of Sound*, vol. 1, Macmillan, 1877.
- [52] W. Thomson, *Theory of Vibration with Applications*, CRC Press, 1996.
- [53] X.Q. Wang, M.P. Mignolet, Stochastic Iwan-type model of a bolted joint: formulation and identification, in: *32nd International Modal Analysis Conference (IMAC XXXII)*, Orlando, FL, 2014.
- [54] B.D. Yang, M.L. Chu, C.H. Menq, Stick-slip-separation analysis and non-linear stiffness and damping characterization of friction contacts having variable normal load, *J. Sound Vib.* 210 (1998) 461–481.